Theoretical and Applied Fracture Mechanics 128 (2023) 104171

Contents lists available at ScienceDirect

Theoretical and Applied Fracture Mechanics

journal homepage: www.elsevier.com/locate/tafmec

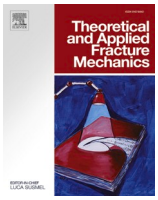

The elasto-plastic numerical study of crack initiation in notched PMMA specimens under uniaxial loading conditions – Tension and torsion

Elżbieta Bura [a,*], Andrzej Seweryn [b]

[a] Faculty of Mechanical Engineering, Bialystok University of Technology, Poland
[b] Faculty of Mechanical Engineering and Ship Technology, Gdansk University of Technology, Poland

ARTICLE INFO

Keywords:
Notches
Plastic strain
Stress–strain fracture criterion
FEM
PMMA
Simple loading condition

ABSTRACT

This paper presents the results of FEM numerical calculations aimed at describing the plastic strain and stress fields under critical loading conditions: tensile force or torsional moment. The calculations were carried out with reference to the results of experimental tensile and torsional tests of flat PMMA specimens weakened with V-notches of different root radii: 0.5, 2 and 10 mm. The procedure for conducting nonlinear numerical analyses is described, including the determination of the actual hardening curve by the hybrid method. A high level of consistency between the results of the experimental and numerical calculations was obtained through description of PMMA with the elastic–plastic material model. The points of occurrence of stress maxima and plastic strain were indicated, which were taken as potential crack initiation sites. On the basis of the stress and plastic strain values measured at the critical points, a stress–strain fracture criterion was formulated, which was then positively verified.

1. Introduction

Today, plastics make up a very large percentage of the materials used in many industries. They are used to make components ranging from those necessary in architecture and aviation to medical materials. The widespread use of plastics such as polymethylmethacrylate (PMMA) brings with it the need to understand its properties under various loading, environmental conditions, including the presence of various types of notches. This type of plastic, in addition to parts made through injection moulding, is most often obtained in the form of a cast or extruded sheets. Thus, components made from PMMA are most often flat discs or blocks. With this, the thickness of these components varies greatly, ranging from 2 to 20 mm. All these factors affect the amount of load a component is able to carry before the final failure. Essentially, estimating the crack initiation moment, allows the safe working conditions to be determined. This is possible, of course, through laboratory experiments, but for environmental reasons, such experiments should take place on a minimum number of samples, and the plastic used in them should be recycled, which is fully possible in the case of PMMA. Prediction of the fracture processes, including critical load values, is possible through analytical and numerical calculations using fracture criteria. In the literature, PMMA functions as a typically brittle material, so researchers most often use classical brittle fracture criteria.

Among the basic methods for predicting fracture processes are energetic criteria. In the work of Seweryn [1], a method for using the Griffith criterion [2] is presented for predicting the critical load value and the propagation direction of an already existing crack. In the work of Seweryn and Łukaszewicz [3], the non-local released energy criterion was used successfully to predict the value of the critical load – the moment of crack initiation in flat PMMA specimens, weakened by sharp V-notches. The accuracy of determining the direction of crack growth using this criterion was not satisfactory enough. Additionally, the strain energy density criterion [4,5] is another relevant energy model. This approach has been developed into a non-local form [6,7] and analysed, among others, in the work of Berto et al. [8].

Currently, the most commonly used tools for predicting the fracture in notched components are stress criteria. Point stress criterion (PS) [9,10] is the stress form of the strain McClintock criterion [11]. The same approach also functions as the maximum tangential stress criterion (MTS) [12]. Subsequent solutions for the MTS criterion are presented in the context of both sharp notches and those with a rounded tip [10,13]. The mean stress criterion (MS) [14,15] was originally used to predict fracture during mode I in the presence of sharp V-notches. This approach was further developed in many work [15–17]. It also took into account

* Corresponding author.
E-mail addresses: e.bura@pb.edu.pl (E. Bura), andrzej.seweryn@pg.edu.pl (A. Seweryn).

https://doi.org/10.1016/j.tafmec.2023.104171
Received 28 August 2023; Received in revised form 31 October 2023; Accepted 1 November 2023
Available online 4 November 2023

the effect of shear stresses. The MS criterion was used to predict the fracture of flat notched specimens [18] and axisymmetric notched specimens [19] under mode III transverse shear conditions. In the work of Gomez et al. [13], the MS criterion was also generalised to the case of U-notched specimens. Criteria using the values of stress intensity factors [20–22] or generalised notch stress intensity factors [23] are also used. Studies of crack initiation in various construction materials, as well as considerations regarding the critical load, can also be found in the works of Bahadori et al. [24], Berto [25], Zappalorto et al. [26], Talebi et al. [27], Arrieta et al. [28] and many other.

The above-discussed relationships are used successfully to predict the fracture processes of plastics under conditions that allow these materials to be described by the equations of linear elastic theory. Amorphous plastics exhibit greater or lesser ductility, which in some cases prevents the direct use of brittle fracture criteria for predicting the critical load value. Torabi et al. [29] described the results for nine fracture experiments conducted on flat specimens made of PMMA-based dental material, weakened with a U-notch of different radii. The parts were tested under tension. The critical force value was effectively estimated using the MTS and MS criteria extended with the equivalent material concept EMC [30]. Torabi et al. refined the proposed concept, and the results also formulated FMC [31] and VMC [32]. The results for three-point bending fracture experiments on V-shaped notched semi-disks (V-SCB) with different notch opening angles are described in Ref. [33].

Analysing the described criteria, it should be noted that the use of numerical calculations is necessary to apply most of them. In the literature on the study of fracture of notched elements made of amorphous plastics, one can find various approaches to FEM modelling. The models vary in terms of the type of finite elements used and the method of describing the material itself. In many works, the shape of the specimens was described by two-dimensional finite elements, usually eight-node finite elements. In each case, the strategic region of the specimen, i.e. the area around the notch bottom, was described with a more dense mesh or special finite elements. The nature of the material was described by experimental values of Young's modulus and Poisson's ratio. The model prepared in this way was used to determine, for example, the crack initiation angles during mode II [34] and surrogate tensile strength values using the previously described EMC [32]. Ongoing research often required the creation of more complicated three-dimensional models. This was mainly due to the need to include the grips used in laboratory tests in the numerical model. In the studies described in papers [18,35–38], linear elastic numerical calculations were carried out on hexagonal elements, usually 20-node elements. In all the cases described above, the handles were assigned perfectly rigid body properties. Bura and Seweryn [39] noted that better coverage of experimental and numerical results for tensile notched specimens is obtained using an elastic–plastic material model and three-dimensional HEX8-type finite elements.

In the work of Chen et al. [40], the results of fracture tests on planar members weakened by a central hole and loaded with an axial tensile force are described. The coupled criterion (CC) of finite fracture mechanics (FFM) was used to predict the failure stress, but the values obtained differed significantly from those determined experimentally. A strong influence of the fracture velocity profile on the value of the critical load was indicated. The same conclusions were indicated in the work by Doitrand et al. [41]. Furthermore, influence of the loading speed on the critical load value during compression of specimens [42] made of PMMA are described in work by Bura et al. [43]. A different approach to the numerical modelling of PMMA is presented in work by Azizi et al. [52]. The paper presents the use of a peridynamic (PD) numerical model to simulate tensile testing of U-and V-notched specimens [39]. Two numerical models were used in the calculations taking into account the brittle and ductile nature of the material elongation. It was observed that the PD-ductile model allows for more accurate results. The need to take into account material nonlinearity when conducting numerical calculations for materials such as PMMA was emphasised as well. The material nonlinearity of PMMA during fracture testing was also taken into account in the studies described in Leite et al. [44]. The coupled stress-energy criterion of finite fracture mechanics (CCFFM) was used to predict the crack initiation moment. In addition to the usual linear elastic (LE) model, the FEM calculations used a nonlinear elastic (NLE) model of the material using the Ramberg-Osgood approximation (using the Newton-Raphson procedure with a larger number of steps). The elements were described in ANSYS software as PLANE82. The approach used achieved a high level of consistency with experimental observations.

This paper presents the procedure for conducting and the results of numerical FEM modelling of stress and plastic strain fields considering the actual material characteristics of polymethylmethacrylate (PMMA) for uniaxial tension and torsion tests of notched parts. The effect of plastic deformation on the crack initiation moment was considered. The material model was described using the real hardening curve determined using the hybrid method, which allowed a very good convergence of experimental data and results of numerical calculations to be obtained. The numerical data were then used to determine the values of critical parameters in the stress–strain fracture criterion. The presented criterion allows the value of the critical load in flat notched specimens made of PMMA working in two simple loading states in tension and in torsion – to be predicted with a high level of accuracy. The presented formula works well regardless of the thickness of the element and the notch root radius.

2. Material and experimental data

The subject of the study is polymethylmethacrylate (PMMA). The polymer used in the study is specified by the trade name PLEXIGLAS®GS (Röhm GmbH) (Table 1). It was obtained in the form of cast sheets with nominal thicknesses of 5 and 15 mm. The selection of significantly different plate thicknesses made it possible to study the influence of this parameter on the crack initiation. In a paper by Bura and Seweryn [45], they describe the results of laboratory fracture tests on flat specimens weakened by notches with different root radii (Fig. 1). Uniaxial tensile and torsion tests (uniaxial loading conditions) were conducted on a MTS 809.10 biaxial testing machine under displacement control of the testing machine's grips. In uniaxial tension, displacement was set at a speed of 0.04 mm/s on a specimen base of 50 mm (ISO 527–1:1993, *Plastics – Determination of tensile properties*, *British Standard*). This yielded an average strain rate of about 0.0008 $s^{-}1$. Each component was stretched until failure. Destroyed examples of the sample are shown in Fig. 2.

The research described in the paper by Bura and Seweryn [45] showed that the strain rate is influenced not only by the speed of setting the rotation angle, but also by the thickness of the specimen. Maintaining the same average strain rate of about 0.0008 s^{-1} as in the case of tensile tests, the rate of the rotation angle change of the gauge base over time was assumed for specimens of nominal thickness $g = 15$ mm equal to$\dot{\phi} = 0.09°/s$, while for specimens of nominal thickness $g = 5$ mm – $\dot{\phi}=$ 0.15 °s. As a result of experimental tests, critical values of tensile force and torsional moment were obtained at which crack initiation was observed. It should be noted that in the case of torsion, the critical load value was not always equal to the maximum value. The critical load

Table 1
PMMA mechanical properties [45].

Property	Value	Unit
Young's modulus E	3254	MPa
Tensile strength R_m	73.88	MPa
Elastic limit $R_{0.05}$	24.51	MPa
Yield stress $R_{0.2}$	47.17	MPa
Failure stress R_u	71.65	MPa
Poisson's ratio ν	0.38	–

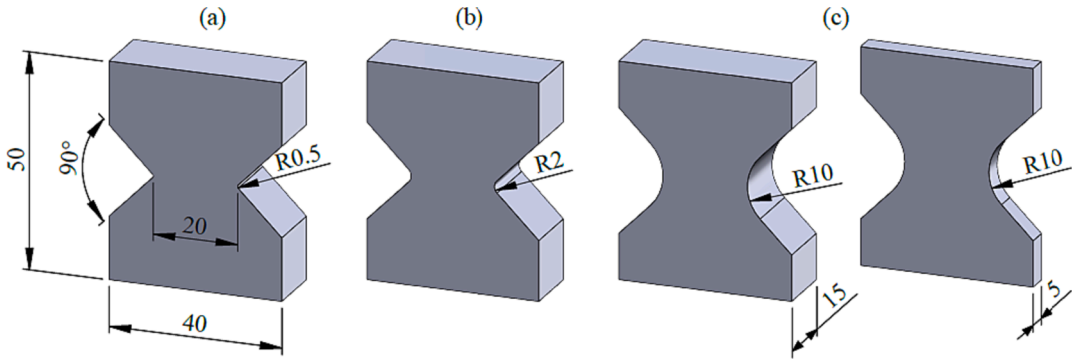

Fig. 1. Specimens used in the study [43]: (a) ρ = 0.5 mm, (b) ρ = 2 mm and (c) ρ = 10 mm with two nominal thicknesses g = 15 mm and g = 5 mm.

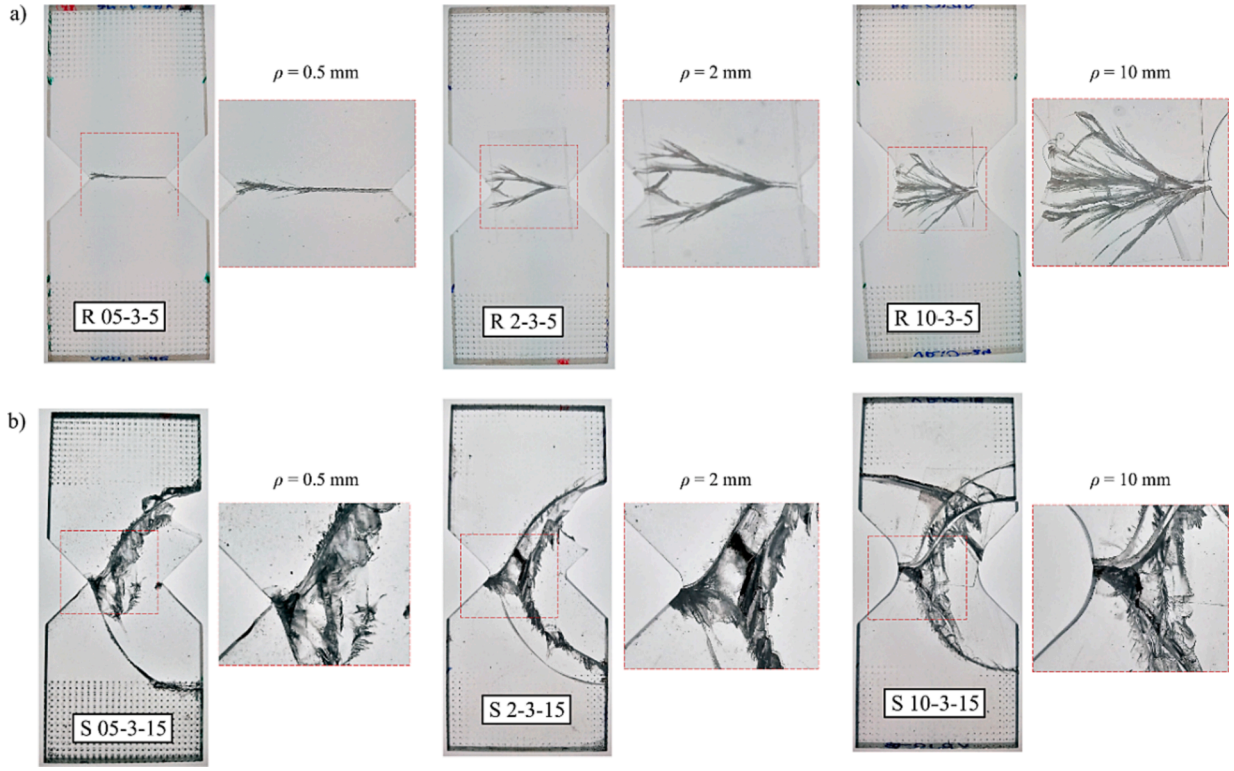

Fig. 2. Specimens (t = 5 mm) after: (a) tensile and (b) torsion tests [45].

Table 2
Critical load values [45].

Tension Specimen	ρ	g	Maximum elongation	Critical force value
	[mm]	[mm]	[mm]	[N]
R-05–5	0.5	4.92	0.24	2.74
R-05–15	0.5	14.38	0.28	8.88
R-2–5	2	4.92	0.45	4.55
R-2–15	2	14.91	0.45	12.94
R-10–5	10	4.91	1.19	7.88
R-10–15	10	14.64	1.20	23.05
Torsion Specimen	P [mm]	g [mm]	Maximum torsional angle [°]	Critical torque value [Nm]
S-05–5	0.5	4.92	31.55	13.94
S-05–15	0.5	14.41	9.03	76.88
S-2–5	2	4.92	29.16	12.92
S-2–15	2	14.18	13.14	80.76
S-10–5	10	4.92	41.79	14.38
S-10–15	10	14.63	25.48	85.09

values (averaged for a given specimen type) are summarised in Table 2, and the tensile and torsional curves for selected specimens are shown in Fig. 3.

3. Numerical calculation

The main objective of this work is to formulate a tool for predicting the crack initiation moment of notched PMMA specimens, operating under uniaxial loading conditions, i.e. subjected to tension or torsion. It was, therefore, necessary to know the stress and strain fields distributions under critical loading conditions near the notch bottom. This goal was achieved by conducting nonlinear numerical calculations using the finite element method. Models and calculations were developed in the MSC Marc Mentat software environment.

3.1. The real hardening curve

An elastic–plastic material model with isotropic hardening role was adopted. The linear elastic range is described by the generalised Hooke's

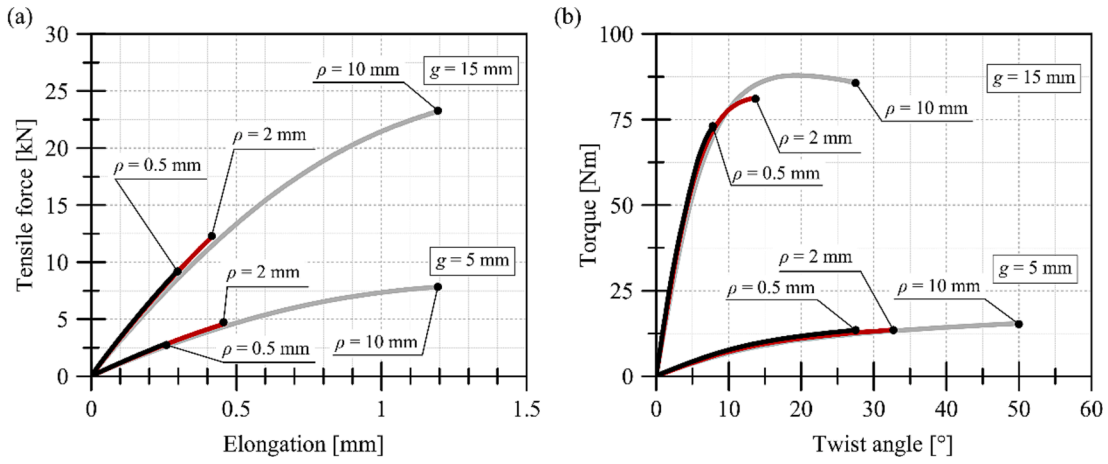

Fig. 3. Experimental curves for (a) tension and (b) torsion tests [45].

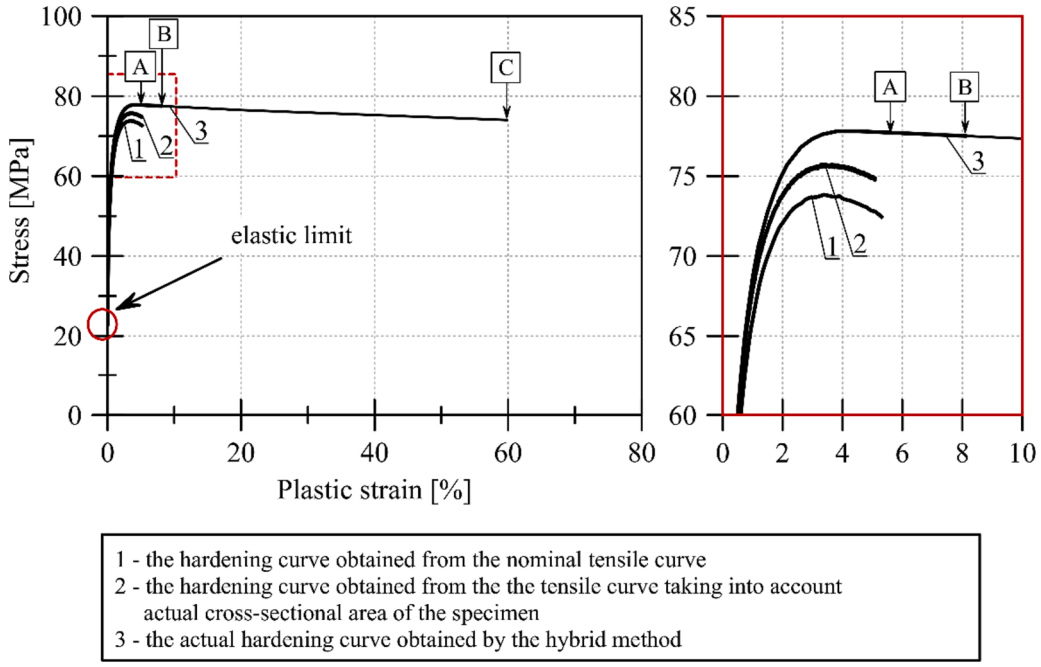

Fig. 4. Hardening curves for PMMA.

law, in which the values of Young's modulus and Poisson's ratio (Table 2) were determined in experimental studies. The relationship between stress and strain in the plastic part was determined by hardening curves (Fig. 4) ascertained from experimental studies. The results for three different hardening curves were verified: (1) the relationship determined from the nominal tensile curve, (2) the relationship determined from the tensile curve taking into account the actual cross-sectional area of the specimen, and (3) the relationship determined by a hybrid method involving the identification of the actual material hardening curve based on iterative FEM calculations aimed at obtaining a correspondence between the force–displacement relationship of the measurement base obtained numerically and experimentally. The starting point in determining the material hardening curve using the hybrid method was the hardening curve obtained for the actual cross-sectional area of the specimen, for which the load and displacement values were determined. Then the results obtained were compared with experimental data. The initial curve was modified in several steps, and the calculation was not completed until the numerical load–displacement curve was matched to the experimental tensile curve. In the present considerations, it is assumed that plastic deformation, which occurs just after the linear range is exceeded, should also be taken into account. Thus, the beginning of the strengthening curve was assigned the value of the elastic limit. It should be noted that the laboratory experiment allowed the range of the hardening curve to reach about 5.5 % plastic strain (Fig. 4 – A).

In order to verify the correctness of the adopted numerical model, preliminary calculations of stress and strain fields on unnotched specimens were carried out. The geometric model and boundary conditions were assumed as in Fig. 5. The area of the specimen located between the grips of the testing machine was assumed for the calculations. For tensile loads using symmetry conditions, only 1/8 of the entire specimen was modelled (Fig. 5). The upper wall of the geometric model was loaded by giving a displacement in the direction perpendicular to it, while on the lower, translation on the load direction was blocked. Translations were received on the remaining walls adjacent to the *zy* and *yz* planes according to the symmetry conditions. As a result of nonlinear numerical calculations, the values of the tensile force as a function of the measurement base displacement were obtained. Calculations were carried out until the values of maximum plastic deformation were reached, respectively, for the given curve. Fig. 6 illustrates the juxtaposition of

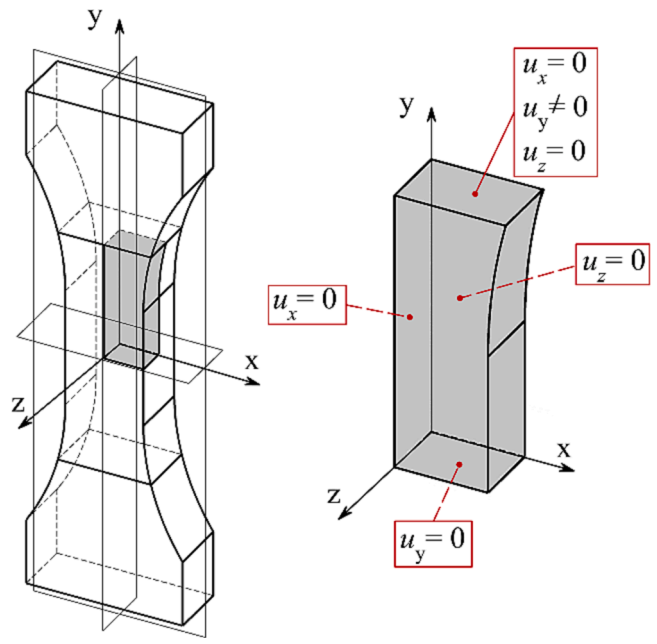

Fig. 5. Boundary conditions for smooth specimen.

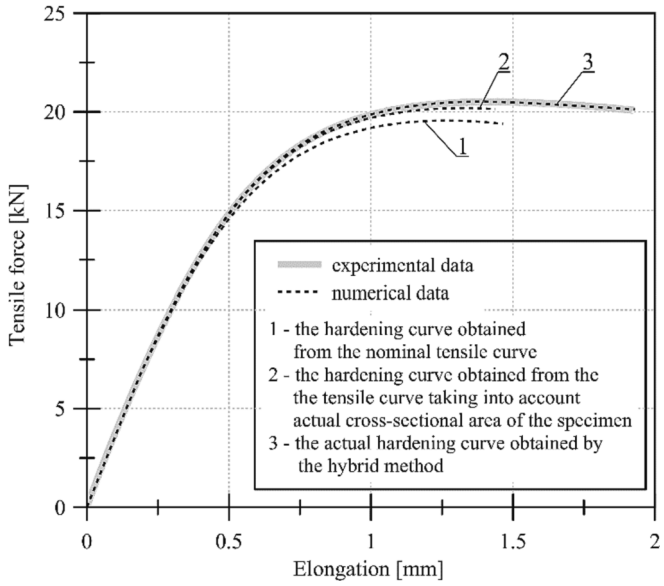

Fig. 6. Experimental and numerical results for a smooth specimen using three different hardening curves.

experimental and numerical results obtained for the three hardening curves shown in Fig. 4. By far the best convergence of results for tensile strain was obtained by modelling the material with the actual hardening curve obtained using the hybrid (iterative) method. With the iterative method, a hardening curve up to about 8.3 % plastic deformation was determined (Fig. 4 – B).

The obtained curve was implemented for numerical calculations of the torsion of a flat notched specimen with a radius of $\rho = 10$ mm (curves obtained for other notches and thicknesses – Fig. 15). A very good overlap between experimental and numerical results up to about 8.3 % plastic strain was obtained. The B-C range (Fig. 4) was again selected using a hybrid (iterative) method. The above enabled the numerical calculations for torsion over the entire range of experimental torsion angle (flat notched specimen with radius $\rho = 10$ mm). The difference in the values of the torque obtained experimentally and numerically when the maximum torsion angle was reached (Fig. 16) is about 2 %.

3.2. Boundary conditions

Numerical calculations conducted on notched specimens subjected to uniaxial tension were carried out on 1/8 of the entire specimen. As in the case of the smooth specimens discussed earlier, using symmetry conditions, the boundary conditions were given as Fig. 7a. Full specimen models were used for torsion analysis. The boundary conditions were set as in Fig. 7b.

3.3. Mesh - convergence of the numerical solve

The selection of a suitable finite element partition mesh began with preliminary numerical calculations in which the nodes were distributed automatically using the tools of the *MSC MARC Mentat* program. It was determined in which areas of the sample the finite element mesh should be densified and in which areas the element size would not affect the result of the calculations. The selection of the finite element size was guided by the relation claiming that the required quality of the HEX element is maintained at a ratio of its smallest and largest dimension at most equal to 1:2. Thus, by dividing the thickness of the sample (the dimension of the thinner sample $g = 4.92$ mm was taken as decisive) into more and more finite elements, their optimal size was determined. In areas where an accurate result was expected, the remaining element dimensions were at most twice as large or smaller. In areas farther away from the critical ones, elements with the largest possible dimensions were used. After building a two-dimensional mesh of four-node QUAD4-type elements, they were transformed into eight-node three-dimensional HEX8-type elements using the *Extrude* tool. The final finite element size was determined based on the convergence of the numerical solution. The finite element describing the notch bottom was of dimension 0.05 mm, 0.141 mm and 0.410 mm respectively for notch with a radius ρ equal to 0.5 mm, 2 mm and 10 mm. Calculations corresponding to tensile tests were carried out until the measurement base maximum elongation was obtained from experimental tests. When the critical load was reached, the maximum principal stress value was read. As the mesh became denser, stabilisation of the stress value was noted. The finite element partition grid was considered optimal and the results were considered good enough when there was no clear change in the value of the monitored quantity in the following compaction step. The above steps were carried out with continuous monitoring of the analysis time. This is another important parameter to consider at this stage of numerical model building. The calculations carried out for the unnotched sample were chosen as an example (Fig. 8). The finite element partition meshes are shown in Fig. 9.

4. Results and discussion

4.1. Tension

As a result of the numerical calculations carried out, the dependence of the tensile force as a function of the measurement base elongation was obtained and compared with the experimental results (Fig. 10). The calculations were conducted by setting the displacement in such a way that the maximum value of the elongation of the measuring base corresponded to its critical value determined experimentally. The relative error of the maximum tensile force and the averaged value of the force obtained experimentally (the value marked "B") for specimens with a nominal thickness of $g = 15$ mm was 3-6 % (Fig. 10a-c), while for specimens with nominal thickness $g = 5$ mm: 0–2 % (Fig. 10d-f). Based on the results obtained, the correctness of the numerical model can be inferred.

In Fig. 11, the distributions of the highest principal stress σ_1 are shown for all tested specimens. The smaller the notch root radius, the

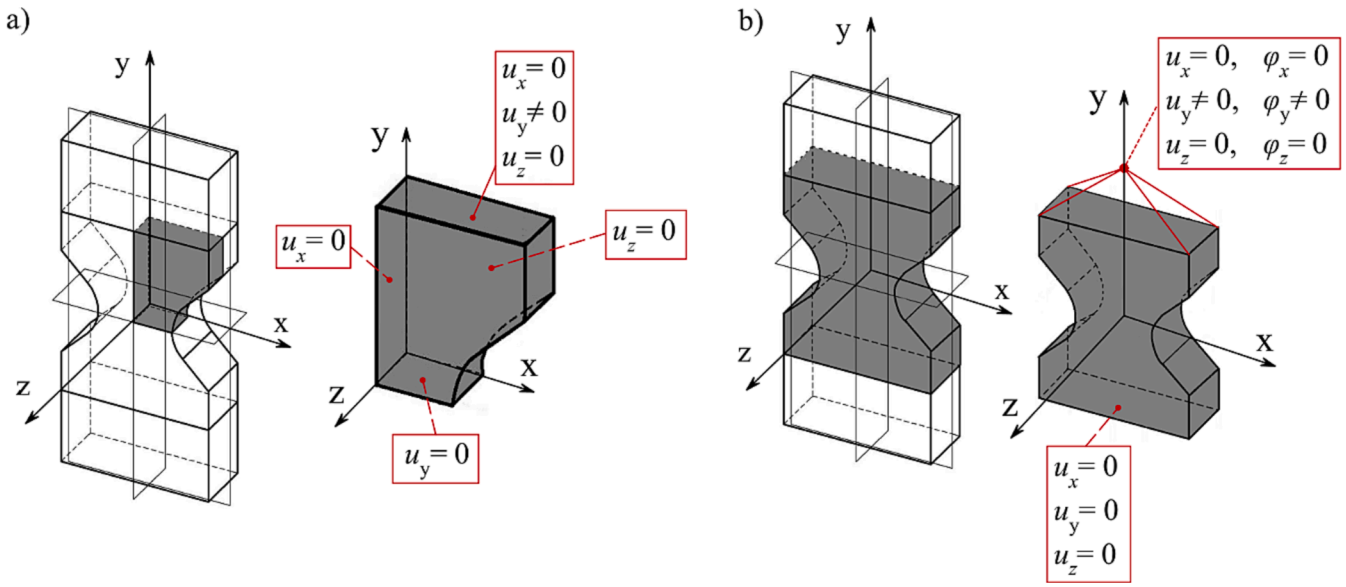

Fig. 7. Boundary conditions used in the calculation of notched samples.

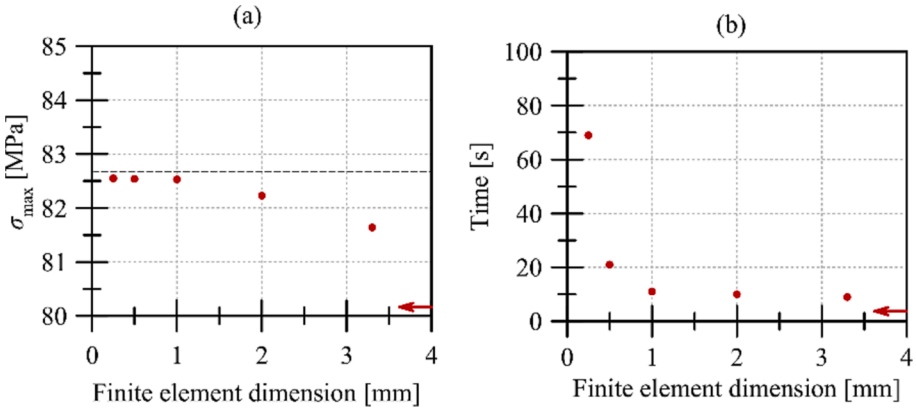

Fig. 8. Convergence of the solution based on the results obtained for smooth (un-notched) specimens: (a) the value of the maximum principal stress as a function of the finite element dimension and (b) the analysis time as a function of the finite element dimension.

higher the stress value. Typical stress concentration near the notch bottom is noted. The stress gradients are higher the smaller the radius ρ is. Fig. 12 shows the distributions of the maximum principal plastic strain ε_1^p. An increase in the notch root radius ρ leads to an increase in the plastic strain, and also to an increase in the yield zone. This is, of course, associated with the higher loads that notched components with larger root radius are able to carry.

The critical area subject to closer analysis is the notch bottom and its vicinity. The maximum principal stress distribution over the specimen thickness at the notch bottom is shown in Fig. 13a. For each specimen, the maximum stress values were almost always reached in the symmetry plane of the specimen xy, i.e. in the centre of the specimen thickness (except when $\rho = 10$ mm and $g = 5$ mm). It is clear that the smaller the radius ρ is, the higher the stress values σ_1. The thickness of the specimen significantly affects the state of stress prevailing in the element. For specimens with a nominal thickness of $g = 5$ mm, the values of analysed stresses are lower than for thicker specimens. The differences in the values obtained for both thicknesses are greater the larger the radius ρ is. For smaller notch root radii ρ, larger stress gradients are observed at the lateral component surface.

Similar trends can be observed in the distribution of maximum plastic strain (Fig. 13b). Again, the greatest differences in the values of maximum strain, for the thinner and thicker specimen, occur for $\rho = 10$ mm. The strain extremum ε_{max}^p always occurs at the notch bottom. The larger the notch root radius, the higher the strain value. For radii of $\rho = 2$ mm and $\rho = 0.5$ mm, similar values of strain ε_{max}^p of about 4–5 % were recorded.

Due to the use of an elastic–plastic material model in the numerical calculations, the stress extremum is not reached at the notch bottom, as would be the case when analysing a linearly elastic material. Fig. 14a shows how the values of stress σ_1 measured at the specimen thickness centre change as a function of distance from the notch bottom. The highest values of normal stress were recorded for the specimen with a radius of $\rho = 0.5$ mm: about 105 MPa and about 97 MPa – for the thicker and thinner specimen, respectively. In other cases, the maximum stresses reached the following values: for $\rho = 2$ mm – about 96 MPa and about 91 MPa, and for $\rho = 10$ mm – about 94 MPa and about 89 MPa. Smaller values were always observed for the thinner sample. The larger the notch root radius ρ, the point at which the stress extremum was recorded is located further from the notch bottom. Thus, these distances (averaged for both thicknesses) are: approx. 0.13 mm, approx. 0.42 mm and approx. 3.49 mm, respectively, at radii $\rho = 0.5$ mm, $\rho = 2$ mm and $\rho = 10$ mm. Thus, the larger the radius, the larger the area in which crack initiation can occur. In fact, this was confirmed by experimental studies, but in the case of specimens with the largest notch root radius $\rho = 10$ mm, the crack initiation site was noted outside the bottom or very close to the notch bottom.

The notch with which the sample was weakened had a smaller

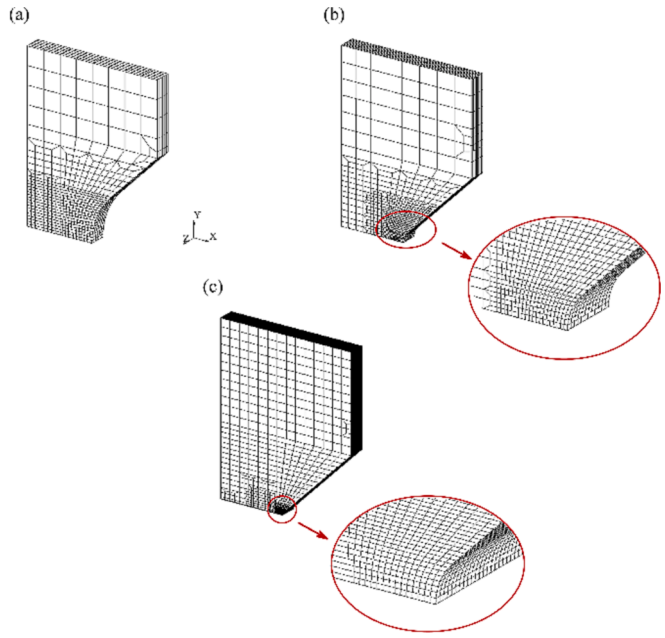

Fig. 9. Finite element meshes shown on 1/8 model for notched specimens with root radius ρ equal to: (a) 10 mm, (b) 2 mm and (c) 0.5 mm.

radius, the greater the stress gradients are noted. For both thin and thick samples, these distributions are very close to each other. The same is true for equivalent stresses σ_{eq}, the distributions of which are shown in Fig. 14b. Again, larger values across the specimen width and smaller stress gradients are observed in notched specimens with the largest bottom rounding radius $\rho = 10$ mm. In the notch bottom, the maximum values of stress σ_{eq} are observed and for all types of samples it is about 78 MPa. Ideally, equivalent stresses at the time of crack initiation should reach the same value, regardless of the specimen thickness and the notch root radius. However, it should be remembered that the stress–strain distributions were established for critical load values determined experimentally, which, however, causes some scatter in the numerical results. It is important to emphasize that the values of equivalent stresses oscillate around a certain specific value, especially in the case of tension. The results will be different the greater the deformation experienced by the component.

For maximum plastic strain ε1p and equivalent plastic strain εpeq, the same values were obtained as a function of distance from the notch bottom (Fig. 15). The strain extremes are always reached at the notch bottom. Regardless of whether the principal or equivalent plastic strain was considered, the same or similar values are referred to. Equivalent strains are expressed on the basis of reducing the case to uniaxial tension, so in the case of tension, the equivalent strains will be equal to the maximum principal strains or will be very close. This is due to the fact that the remaining strain components are very small in value. The largest values were recorded for the specimens with the largest notch root radius $\rho = 10$ mm. For the other two radii, the values of maximum strain are similar to each other. In most cases, higher values of plastic strain were obtained for specimens with a nominal thickness of $g = 5$ mm (the only exception is the case of $\rho = 0.5$ mm). The further away from the notch bottom, the lower the strain values. For small radii $\rho = 0.5$ mm and $\rho = 2$ mm, for the vast majority of the analysed section, they oscillate around zero – a small yield zone. The values of strain and stress obtained by means of numerical calculations, determined at the points where their extremes were recorded, will be used later in the work to formulate the stress–strain fracture criterion.

Similar is the case with the values of equivalent stresses (it should be emphasized that they are presented in the paper only indicatively - they were not used in the final version of the fracture criterion). Ideally, equivalent stresses at the time of crack initiation should reach the same value, regardless of the specimen thickness and the notch root radius. However, it should be remembered that the stress–strain distributions were established for critical load values determined experimentally, which, however, causes some scatter in the numerical results. It is important to emphasize that the values of equivalent stresses oscillate around a certain specific value, especially in the case of tension. The results will be different the greater the deformation experienced by the component. Unfortunately, during the experiment, as the torsion angle in particular increases, changes occur in the material, which also affect the result obtained.

4.2. Torsion

The torque was set by controlling the angular displacement until the maximum torsion angle of the gauge base determined by experimental tests was reached. As a result of numerical calculations, the dependence of the torque as a function of the gauge base twist angle was obtained and compared with experimental results (Fig. 16). High convergence of numerical and experimental results was obtained. The relative error of the critical torque value and the averaged critical torque value obtained experimentally (the value marked "B") for specimens with nominal thickness $g = 5$ mm is 3–6 % (Fig. 16a-c), while for specimens with nominal thickness $g = 15$ mm: 2–6 % (Fig. 16d-f). Based on the results obtained, the correctness of the numerical model can be inferred.

In Fig. 17, the distributions of the maximum principal stress σ_1 are shown for all the specimens tested experimentally. Typical stress concentration in the region of the notch bottom is noted, which is more intense the smaller the radius ρ is. In the case of torsion, the place of stress concentration occurs near the lateral specimen surface. The specimen thickness does not significantly affect the stress value σ_{max}, which, for the same notch root radius ρ, but different specimen thicknesses, remains at a similar level.

Fig. 18 shows the maximum principal plastic strain ε_1^p distributions. The larger the notch root radius ρ, the smaller the value of plastic strain ε_{max}^p, but at the same time the larger the yield zone. The highest strain values were observed in notched specimens with a radius of $\rho = 0.5$ mm. Nodes, where the maximum values of normal stress σ_{max} and plastic strain ε_{max}^p, occurred had different locations depending on the notch root radius and the specimen thickness. Experimental studies proved that during torsion, the crack initiation surface was located near the notch bottom and the lateral specimen surface. In addition, the crack never initiated from points lying on the notch symmetry plane. Similar conclusions can be drawn from the analysis of the results of numerical calculations. Table 3 describes the location of the points where the maximum values of normal stress σ_{max} and the maximum values of plastic strain ε_{max}^p occurred, where: x_m – the distance of the point from the notch bottom and z_m – the distance of the point from the specimen edge measured on a plane parallel to the notch symmetry plane and offset by y_m (Fig. 19).

Locating the maximum values of stress σ_{max} and plastic strain ε_{max}^p locations made it possible to predict the crack initiation locations and to compare these points with those obtained experimentally. The changes in stress σ_1 were determined after the specimen thickness and after the distance between notches for specimens with nominal thickness $g = 5$ mm (Fig. 20a,b) and $g = 15$ mm (Fig. 20c,d). In the diagrams, the grey box indicates the experimental limit of the crack initiation surface determined from dimensions taken from microscopic images of fracture surfaces [45].

For specimens with thickness $g = 5$ mm, the maximum normal stress value σ_{max} after specimen thickness is not reached at the same point for each radius ρ (Fig. 20a). It always occurs near the experimentally determined location of crack initiation. For radius $\rho = 10$ mm, the maximum stress σ_{max} occurs at the side wall of the specimen, while for other radii it is about 1 mm away from the side wall. After the maximum is reached, a clear decrease in the stress value is observed along the

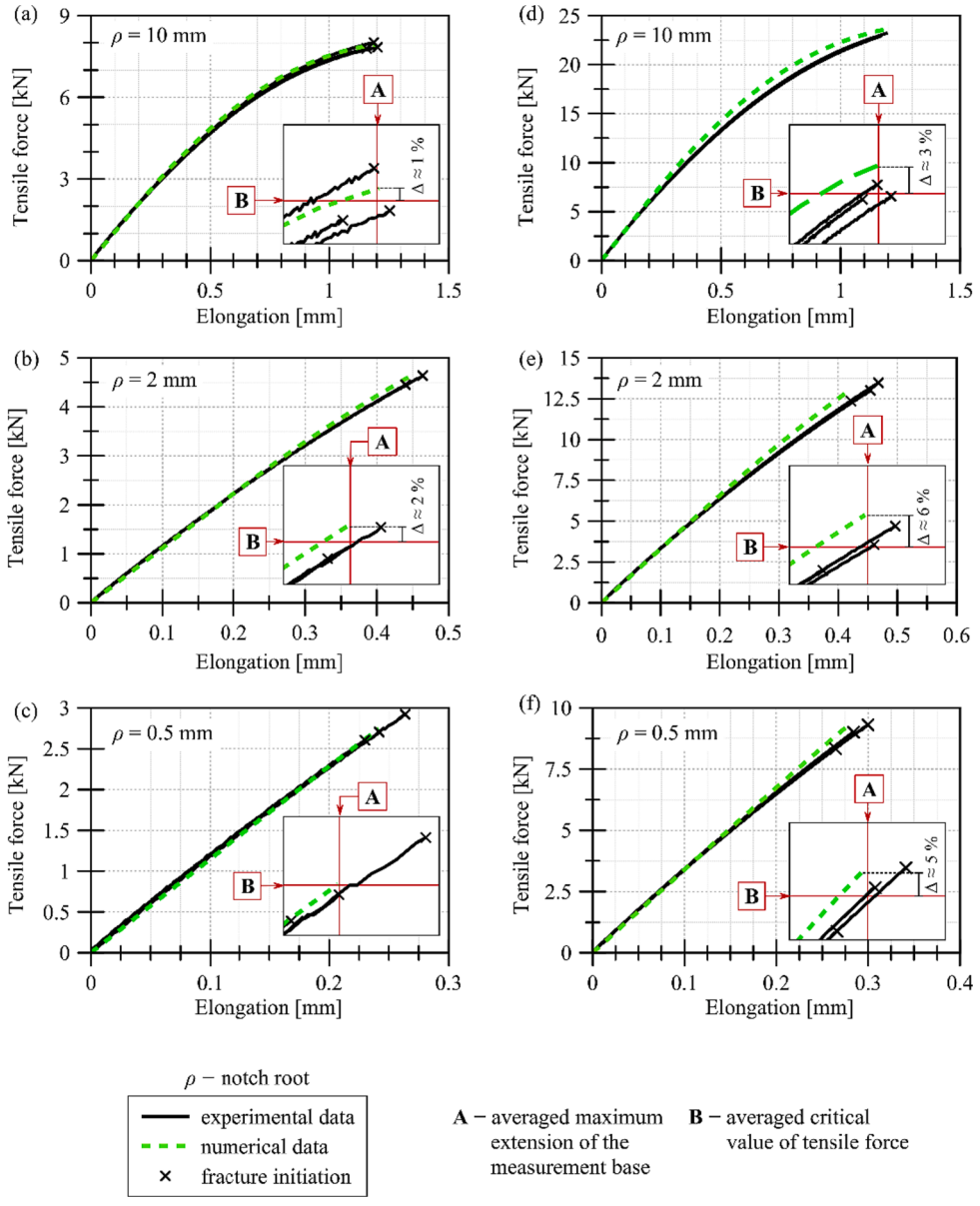

Fig. 10. Tensile curves of notched specimens with nominal thickness g = 5 mm (a)-(c) and for g = 15 mm (d)-(f), black – experimental data [43], green – numerical results. (For interpretation of the references to colour in this figure legend, the reader is referred to the web version of this article.)

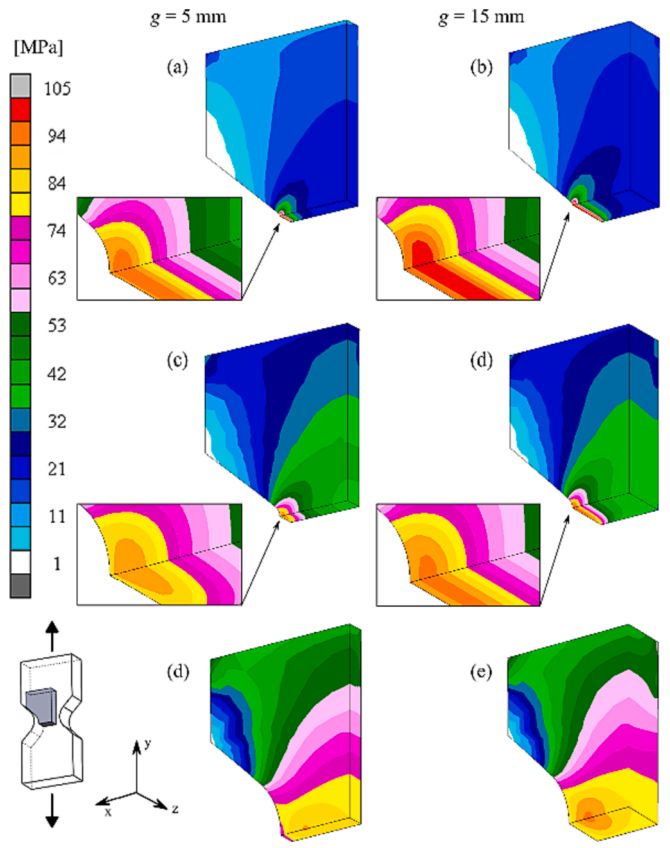

Fig. 11. Distributions of the maximum principal stress σ_1 for notched specimens with a root radius ρ equal to: (a), (b) 0.5 mm, (c), (d) 2 mm and (e), (f) 10 mm.

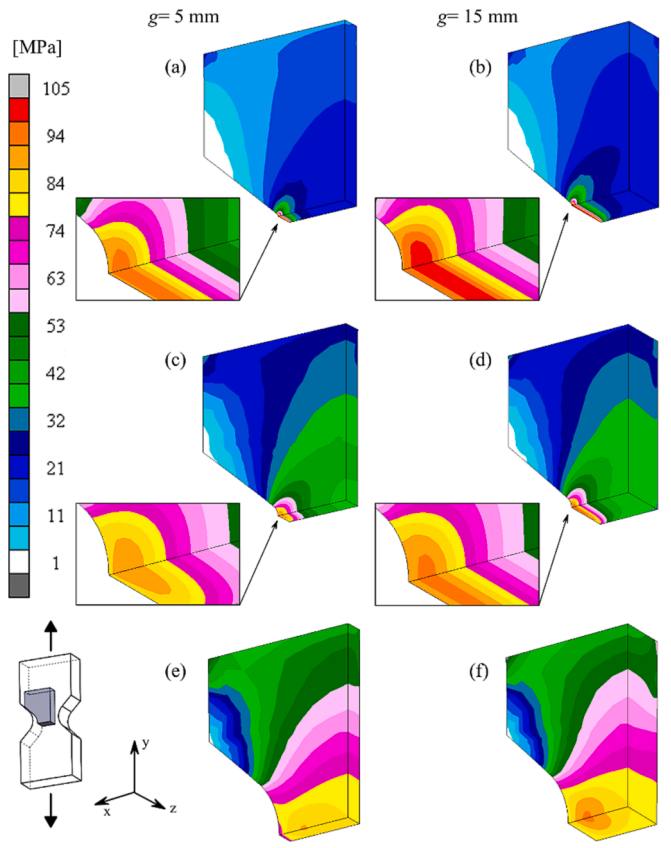

Fig. 12. Distributions of the maximum principal plastic strain ε_1 for notched specimens with a root radius ρ equal to: (a), (b) 0.5 mm, (c), (d) 2 mm and (e), (f) 10 mm.

specimen thickness. Similar distributions of this value were observed as a function of distance from the notch bottom (Fig. 20b). The maximum σ_{max} was recorded at the notch bottom. These points are again adjacent to the crack initiation surface determined experimentally. After reaching the maximum value, the stresses decrease and reach similar values in the specimen centre. For specimens with a nominal thickness of $g = 15$ mm, the relationships are similar to the previous ones. The larger the radius ρ, the maximum stress occurs closer to the side wall of the specimen (Fig. 20c). Only in the case of $\rho = 10$ mm does the point of occurrence of the maximum normal stress σ_{max} coincide with the experimental location of crack initiation. In other cases, the points of occurrence of σ_{max} are slightly away from it – about 0.5 mm from the boundary of the crack initiation surface. The σ_1 distributions along the notch spacing of specimens with nominal thickness g = 15 mm (Fig. 20d) confirm microscopic observations [45] – since each of the normal stress maxima is located in the area of the experimental crack initiation surface. Analysis of the calculation results leads to the conclusion that the stress maxima σ_{max} are largely responsible for crack initiation during torsion of flat notched specimens.

Additionally, it was analysed how the maximum plastic strain values ε^p_{max} change as a function of distance from the notch bottom for specimens with nominal thickness $g = 5$ mm (Fig. 21a,b) and $g = 15$ mm (Fig. 21c,d). Only for specimens with $\rho = 0.5$ mm, the maximum strain ε^p_{max} was recorded near the lateral specimen surface (Fig. 21a, Fig. 21c). The larger the radius ρ, the point of occurrence of the maximum is moved further away from the experimentally determined crack initiation surface. In the case of thinner specimens with the largest notch root radius, this point was recorded at the very centre of the specimen thickness (green circle - Fig. 21). The maximum value of plastic strain ε^p_{max} for both thicknesses was always located at the notch bottom (Fig. 21b, Fig. 21d), which coincides with experimental observations [45]. The region around the notch bottom is also characterised by large gradients in strain values. As the distance from the notch bottom increases, the principal plastic strain value ε^p_1 decreases and for all notch radii ρ converges to similar values.

5. Fracture criterion

As a result of the numerical calculations, the distributions of stresses and strains under critical loading conditions causing crack initiation were obtained. The calculations made it possible to identify the locations of the maximum principal stress σ_{max} and the maximum principal plastic strain ε^p_{max} values. These locations were considered potential sites of crack initiation, and the obtained data were used to formulate various forms of the fracture criterion. The values of stress σ_1, σ_{eq} and the corresponding values of plastic strain ε^p_1, ε^p_{eq} measured at the point of occurrence of maximum stress σ_{max} and maximum plastic strain ε^p_{max} at the time of crack initiation in tension were tabulated (Table 4 and Table 5) and during torsion (Table 6 and Table 7).

Each loading case was considered separately. The maximum principal stress and the maximum principal plastic strain values measured at the points of occurrence of maximum normal stress and plastic strain obtained from numerical calculations of tensile notched specimens are shown in Fig. 22. It was determined in which cases the location of the maximum stress σ_{max} or plastic strain ε^p_{max} coincides (or is close) with the experimentally verified location of the crack initiation site (red crosses). Then the data from these points were adopted to the local stress–strain fracture criterion, presented earlier in the work of Bura and Seweryn [45].

The proposed criterion assumes that normal stress and plastic strain (the maximum principal or equivalent) are responsible for crack initiation, which affect the material's resistance to fracture. The higher the

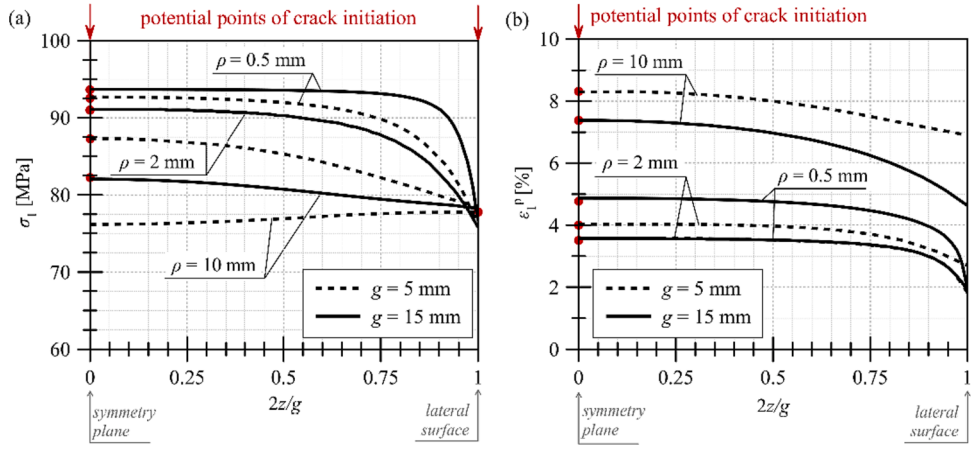

Fig. 13. (a) The maximum principal stress σ_1 at the bottom of the and (b) the maximum principal plastic strain ε_1^p at the bottom of the notch (z - distance from the symmetry plane of the specimen, g - nominal thickness of the specimen).

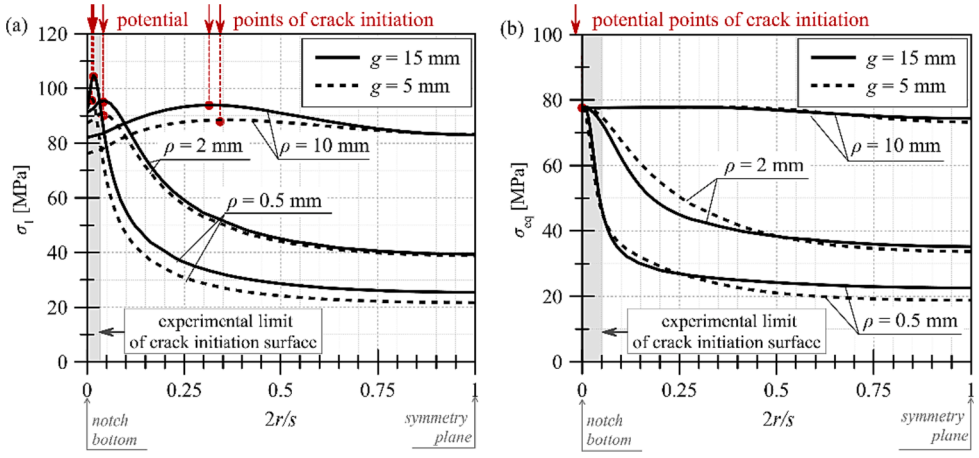

Fig. 14. (a) The maximum principal stress σ_1 and (b) the equivalent stress σ_{eq} at the centre of the specimen thickness (r - distance from the notch bottom, s - distance between notches).

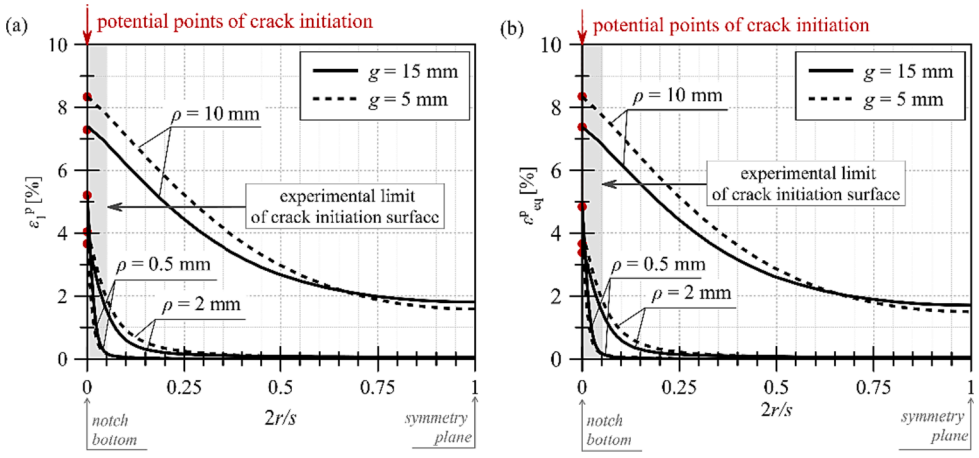

Fig. 15. (a) The maximum principal plastic strain ε_1 and (b) the equivalent plastic strain ε_{eq} at the centre of the specimen thickness (r - distance from the notch bottom, s - distance between notches).

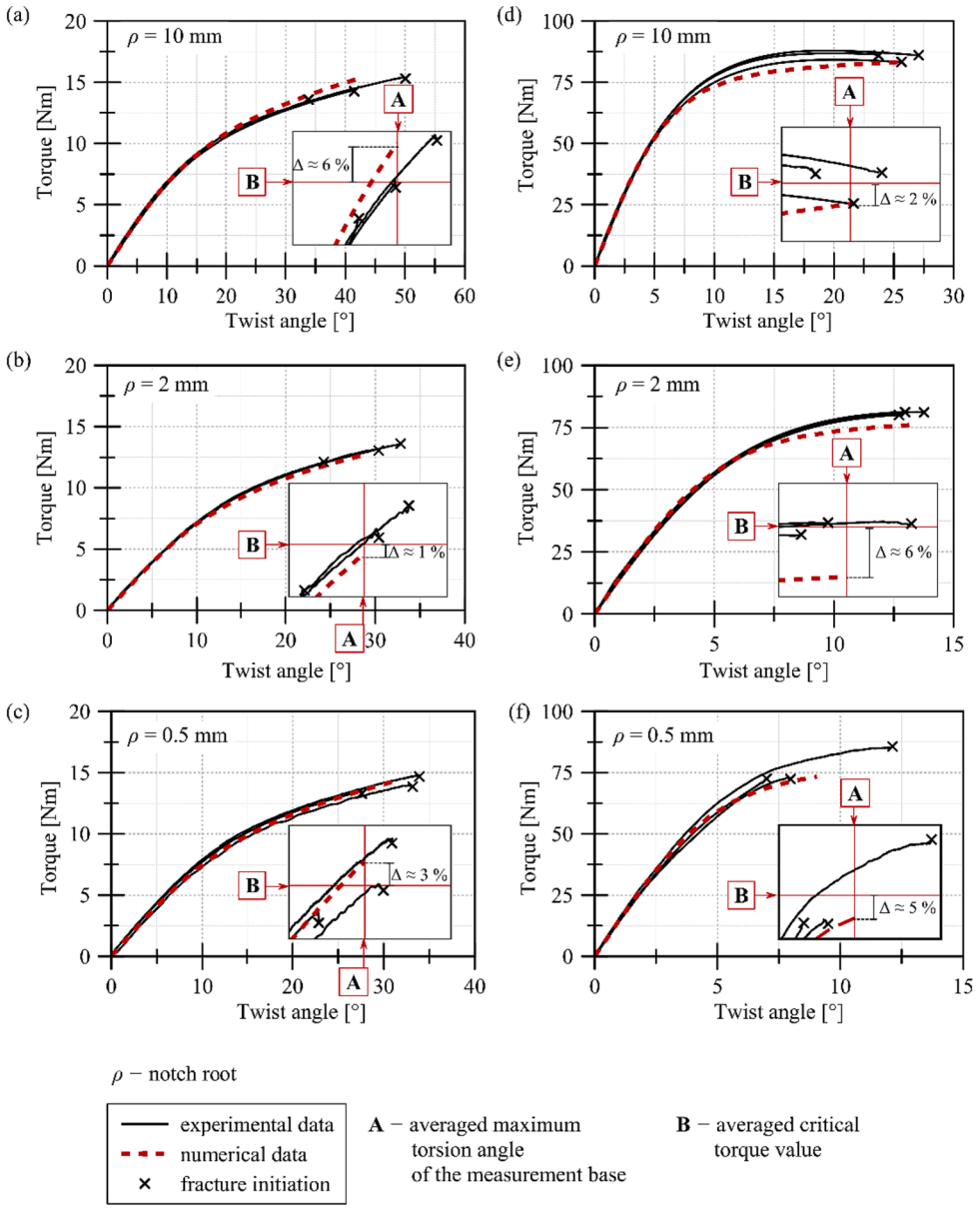

Fig. 16. Torsion curves of notched specimens with nominal thickness g = 5 mm (a)-(c) and for g = 15 mm (d)-(f), black – experimental data [43], red – numerical results. (For interpretation of the references to colour in this figure legend, the reader is referred to the web version of this article.)

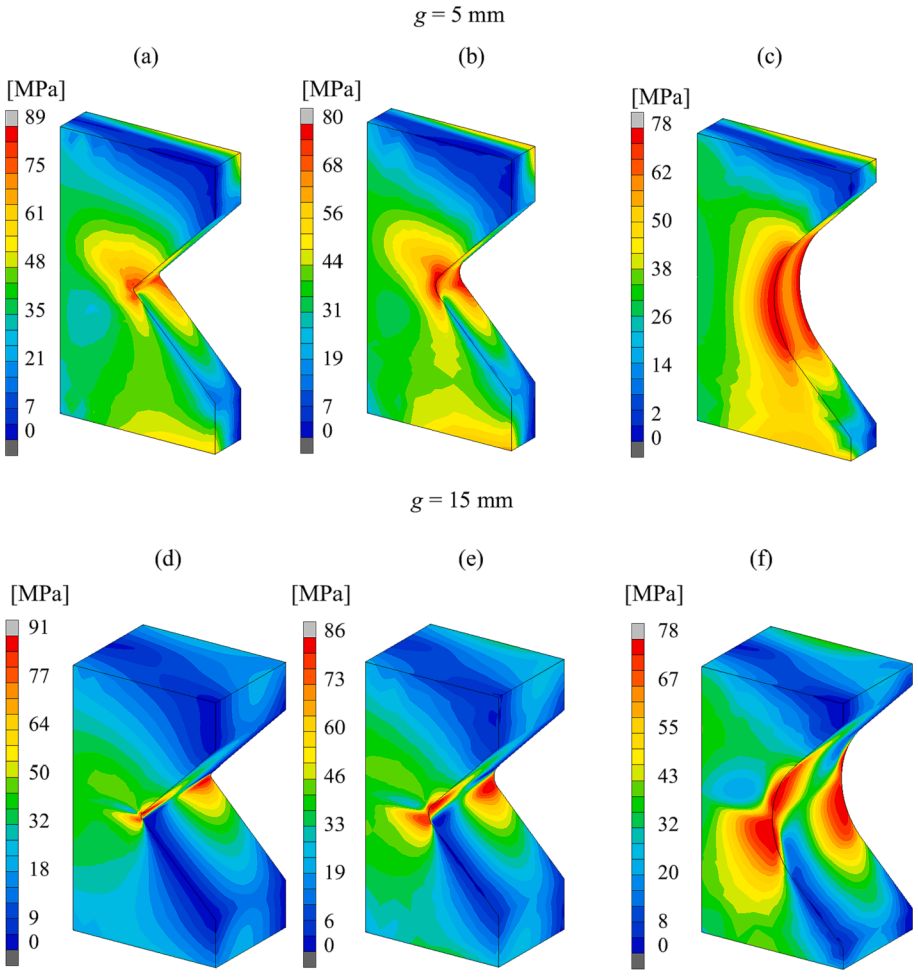

Fig. 17. The maximum principal stress σ_1 for notched specimens with root radius ρ equal to: (a), (d) 0.5 mm, (b), (e) 2 mm and (c), (f) 10 mm (torsion).

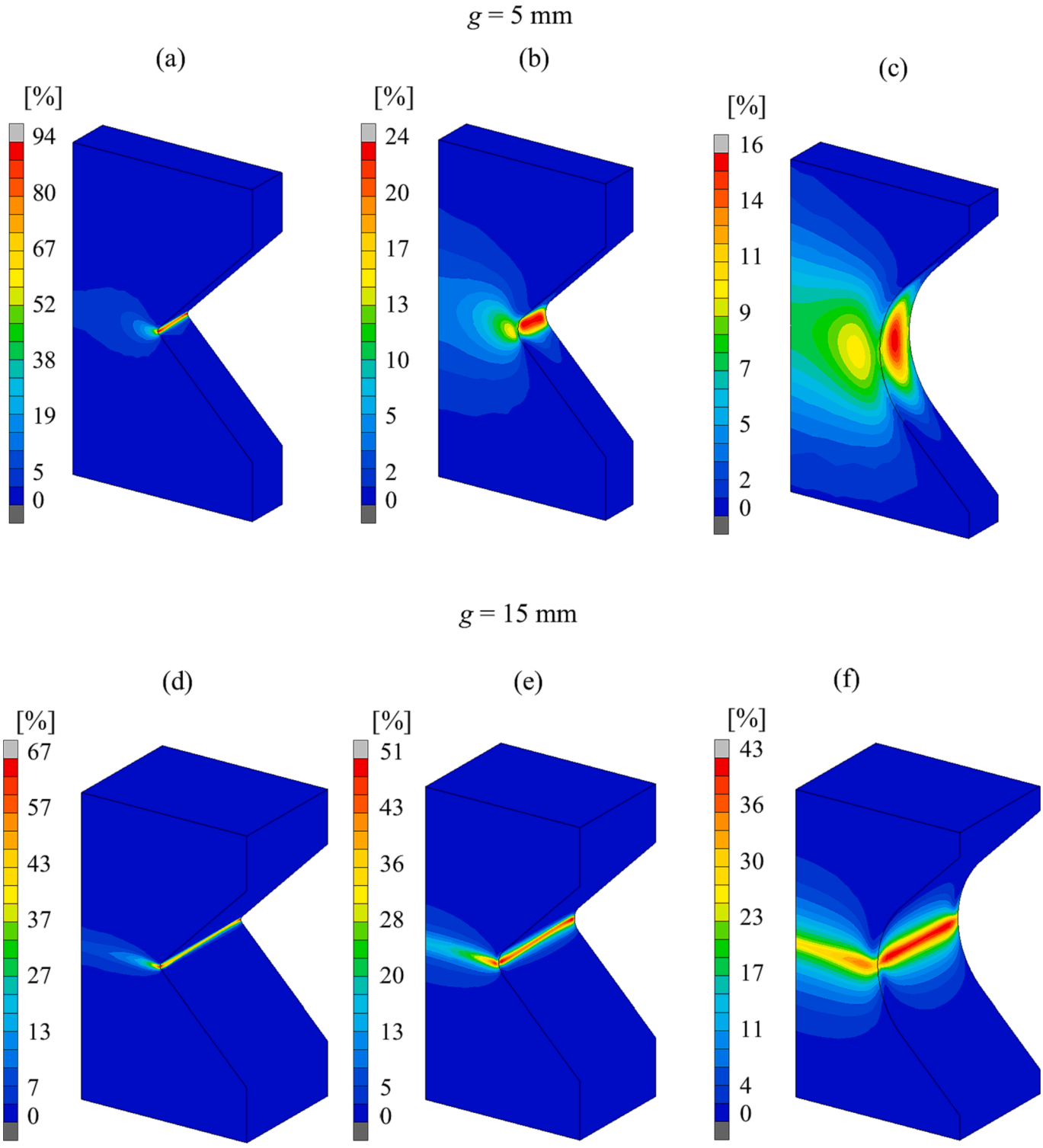

Fig. 18. The maximum principal plastic strain ε_1^p for notched specimens with root radius ρ equal to: (a), (d) 0.5 mm, (b), (e) 2 mm and (c), (f) 10 mm (torsion).

Table 3
The stress and strain maxima location points.

ρ [mm]	g [mm]	σ_{max}			ε^p_{max}		
		x_m	y_m	z_m	x_m	y_m	z_m
0.5	4.92	0.61	0.23	0.67	0	0	0.21
	14.5	0.12	−0.32	1.12	0	0.05	0.15
2	4.92	0.98	1.26	0.62	0	−0.20	1.03
	14.5	0	−1.11	1.35	0	0	0.41
10	4.92	0	4.39	0	0	0	2.46
	14.5	0.56	−2.02	0	0	0	4.56

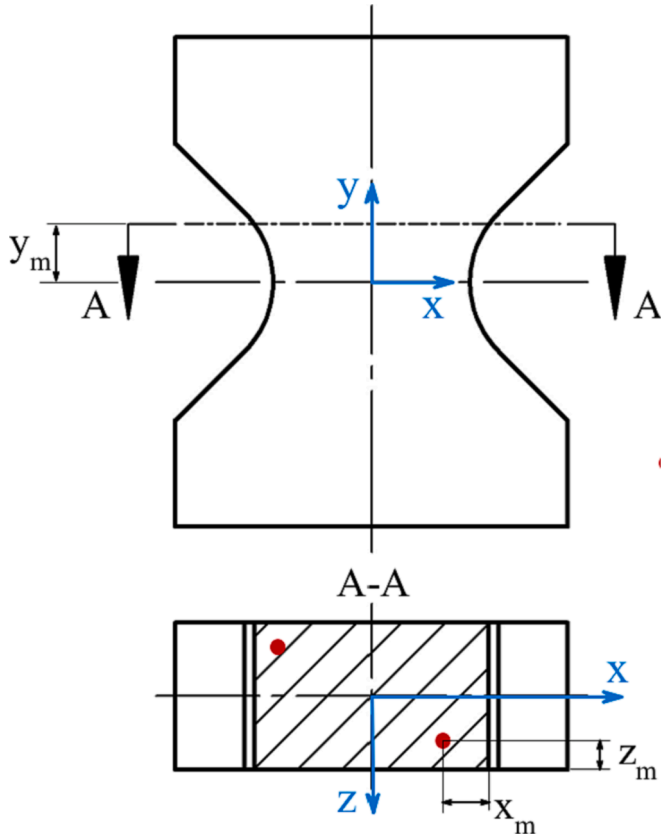

Fig. 19. Location points of maximum values of monitored quantities: σ_{max}, ε^p_{max}.

level of plastic strain, the lower the resistance. Thus, the stress–strain criterion for fracture in this case can take a form similar to the solution proposed by Seweryn and Mróz [16,46]:

$$\max_{(n,x_0)}\frac{\sigma_n}{\sigma_c} = \max_{(n,x_0)}\frac{\sigma_n}{\sigma_{c0}(1-\omega)} = 1 \tag{1}$$

where: σ_n – the normal stress on the physical plane, σ_c – the failure stress in the damaged material, σ_{c0} – the failure stress in the undamaged material, x_0 – the vector defining the location of crack initiation, n – the vector normal to the physical plane. The damage variable ω can be described as the ratio of the value of the highest plastic strain ε^p_1 (or equivalent plastic strain ε^p_{eq}) and the critical value of plastic strain ε_c, namely:

$$\omega = \frac{\varepsilon^p_1}{\varepsilon_c} \tag{2}$$

or

$$\omega = \frac{\varepsilon^p_{eq}}{\varepsilon_c} \tag{3}$$

The above-described relationships were successfully used to predict fracture in cylindrical specimens made of EN-AW 2024 aluminium alloy and weakened with notches [47–49]. The concept was also developed taking into account the effect on the fracture process of elevated temperature [50,51]. In the work of Bura and Seweryn [39], a study of fracture prediction in tensile PMMA specimens (elements with nominal thicknesses of 10 and 18 mm weakened with V-and U-notches) based on the same relationships is described. In this paper, the critical stress and plastic strain values were determined based on the results obtained for all specimens, including the unnotched specimen, and these parameters took the values: $\sigma_c = 98.89$ MPa and $\varepsilon^p_c = 0.349$.

In the stress–strain fracture criterion, crack initiation is assumed to occur when the maximum principal stress σ_1 reaches a critical value σ_c dependent on the maximum principal ε^p_1 or equivalent plastic strain ε^p_{eq}. Thus, the criterion takes the form:

$$\sigma_1 = \sigma_c = \sigma_{c0}(1 - \frac{\varepsilon^p_1}{\varepsilon_c}) \tag{4}$$

or.

$$\sigma_1 = \sigma_c = \sigma_{c0}(1 - \frac{\varepsilon^p_{eq}}{\varepsilon_c}) \tag{5}$$

In order to use the criterion in question, it is necessary to know the distributions of stresses and plastic strain obtained by nonlinear numerical calculations, taking into account the fact that the first plastic strain occurs already after the elastic limit $R_{0.05}$ is exceeded. The critical values of the parameters σ_{c0} and ε_c determined for the data obtained in tensile tests (Fig. 22) are:

$\sigma_{c0} = 106.19$ MPa, $\varepsilon_c = 0.2832$,
$\sigma_{c0} = 106.53$ MPa, $\varepsilon_c = 0.2816$.

It should be noted that in the case of tensile, prediction of crack initiation moment of specimens of different thickness weakened by notches (with different notch root radius) – regardless of whether the value of the maximum principal plastic strain ε^p_1, or the equivalent strain ε^p_{eq} is used to describe the damage variable – the form of the criterion will be very similar. The values of the obtained critical parameters used in the criterion are similar to those determined in the work of [39]. It should be noted that the two PMMA tested, despite the same technology for the manufacture of the plates and the same manufacturer, differ in their properties at least in the value of Young's modulus, which consequently affects the resistance of the material in question to fracture and thus the values of the critical parameters. It is concluded that accurate fracture testing of plastic elements should be preceded by the determination of the mechanical and strength properties of a given material. Generic values contained in material databases should not be used, as many factors contribute to the fact that material from the same batch may have different properties.

The approach described above was applied to torsion (Fig. 23). The critical values of stress σ_{c0} and plastic strain ε_c were for torsion:

$\sigma_{c0} = 85.98$ MPa, $\varepsilon_c = 27420$,
$\sigma_{c0} = 86.43$ MPa, $\varepsilon_c = 2.7145$.

The criteria proposed for single loading conditions were verified, and the verification results in the form of relative error between the stress value obtained σ_c from the criterion and the value obtained from numerical calculations are summarised in Table 8. The errors were calculated only for those points that were considered as potential crack initiation sites (marked in red in Fig. 22 and Fig. 23).

For uniaxial tension, the average relative error is about 3 %, while for torsion it is 12 % (the lower and upper error limits are plotted on each graph – blue dashed line, Fig. 22 and Fig. 23). For elements in tension, the proposed criterion will work regardless of whether the stress–strain

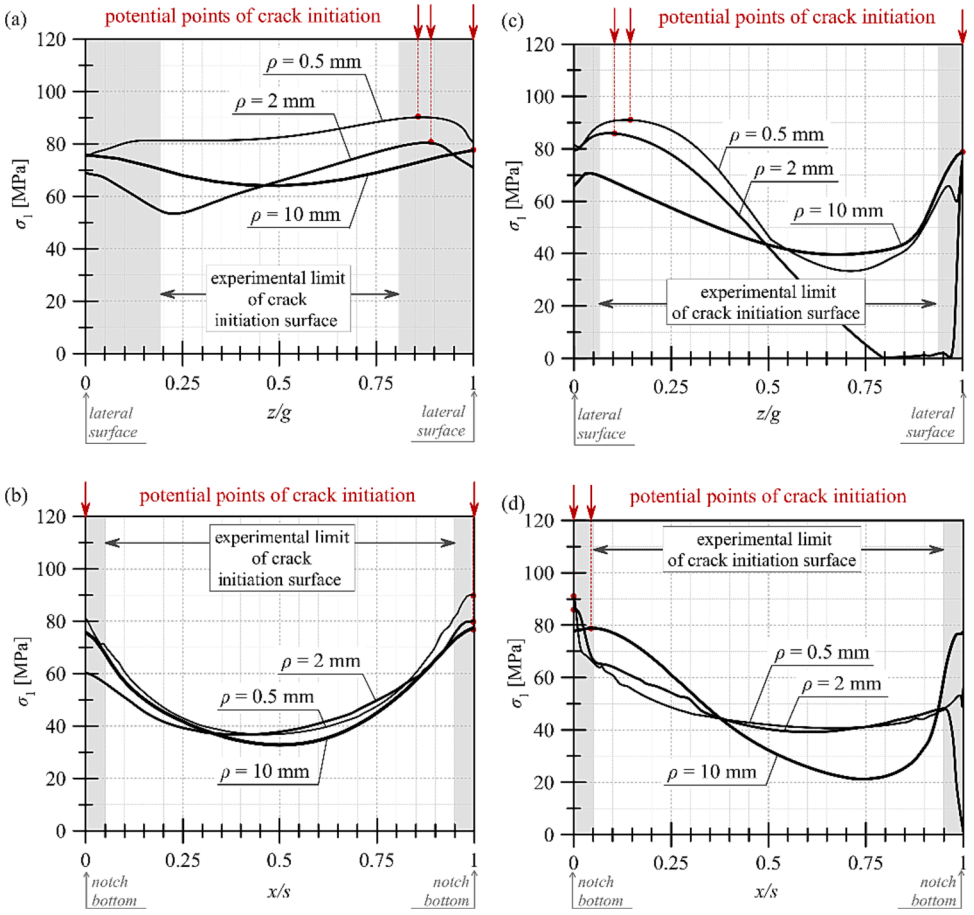

Fig. 20. The maximum principal stress σ_1 distribution for specimens with nominal thickness $g = 5$ mm: (a)-(b) and for $g = 15$ mm: (c)-(d) for x_m, y_m, z_m where: z - distance from the specimen lateral surface, g - nominal specimen thickness, r - distance from the notch bottom, s - distance between notches.

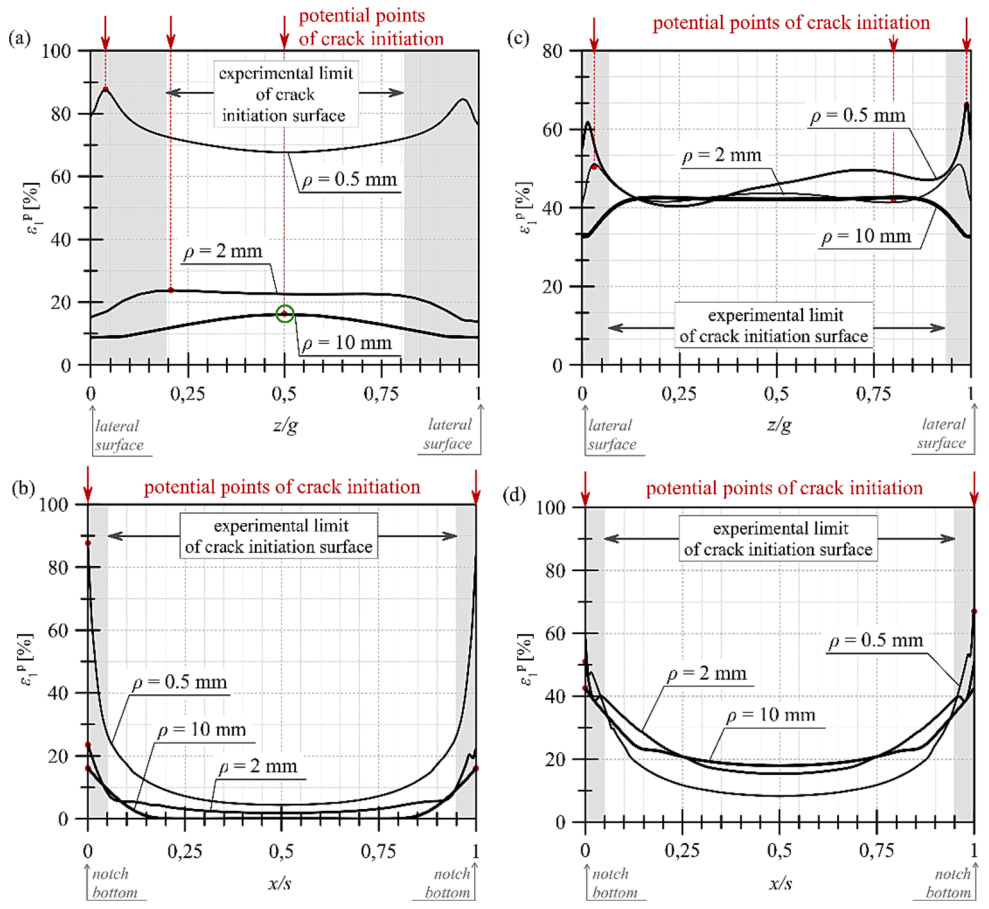

Fig. 21. The maximum principal plastic strain ε_1 distribution for specimens with nominal thickness $g = 5$ mm: (a)-(b) and for $g = 15$ mm: (c)-(d) for x_m, y_m, z_m where: z - distance from the specimen lateral surface, g - nominal specimen thickness, r - distance from the notch bottom, s - distance between notches.

Table 4
Values of stress σ_1, σ_{eq} and corresponding plastic deformation ε_1^p, ε_{eq}^p measured at the point of stress maximum value σ_{max} at the initiation moment – tension.

ρ [mm]	g [mm]	Stress [MPa]		Plastic strain [%]	
		σ_{max}	σ_{eq}	ε_1^p	ε_{eq}^p
0.5	4.92	96.71	74.44	1.79	1.82
0.5	14.5	104.78	74.63	1.80	1.8
2	4.92	90.74	75.55	2.10	2.10
2	14.5	95.54	73.94	1.69	1.71
10	4.92	88.52	77.81	3.89	3.99
10	14.5	93.95	77.77	3.69	3.73

Table 5
Values of stress σ_1, σ_{eq} and corresponding plastic deformation ε_1^p, ε_{eq}^p measured at the point of plastic strain maximum value ε_{max}^p at the initiation moment – tension.

ρ [mm]	g [mm]	Stress [MPa]		Plastic strain [%]	
		σ_1	σ_{eq}	ε_{max}^p	ε_{eq}^p
0.5	4.92	92.70	77.87	3.59	3.74
0.5	14.5	93.69	77.80	4.87	5.22
2	4.92	87.30	77.88	4.03	4.07
2	14.5	91.15	77.83	3.57	3.71
10	4.92	76.16	77.49	8.34	8.35
10	14.5	82.05	77.56	7.38	7.41

Table 6
Values of stress σ_1, σ_{eq} and corresponding plastic deformation ε_1^p, ε_{eq}^p measured at the point of stress maximum value σ_{max} at the initiation moment – torsion.

ρ [mm]	g [mm]	Stress [MPa]		Plastic strain[%]	
		σ_{max}	σ_{eq}	ε_1^p	ε_{eq}^p
0.5	4.92	90.18	75.80	28.15	30.01
	14.5	91.01	77.26	10.12	10.19
2	4.92	80.41	77.55	6.32	6.46
	14.5	85.95	77.52	8.48	8.52
10	4.92	77.63	78.18	4.33	4.34
	14.5	78.90	76.10	14.90	15.00

Table 7
Values of stress σ_1, σ_{eq} and corresponding plastic deformation ε_1^p, ε_{eq}^p measured at the point of plastic strain maximum value ε_{max}^p at the initiation moment – torsion.

ρ [mm]	g [mm]	Stress [MPa]		Plastic strain [%]	
		σ_1	σ_{eq}	ε_{max}^p	ε_{eq}^p
0.5	4.92	72.93	71.67	87.37	87.41
	14.5	74.95	73.04	66.69	67.04
2	4.92	68.37	76.24	23.75	24.47
	14.5	76.71	73.78	51.11	51.44
10	4.92	62.43	76.72	16.16	17.34
	14.5	55.20	74.84	42.63	46.56

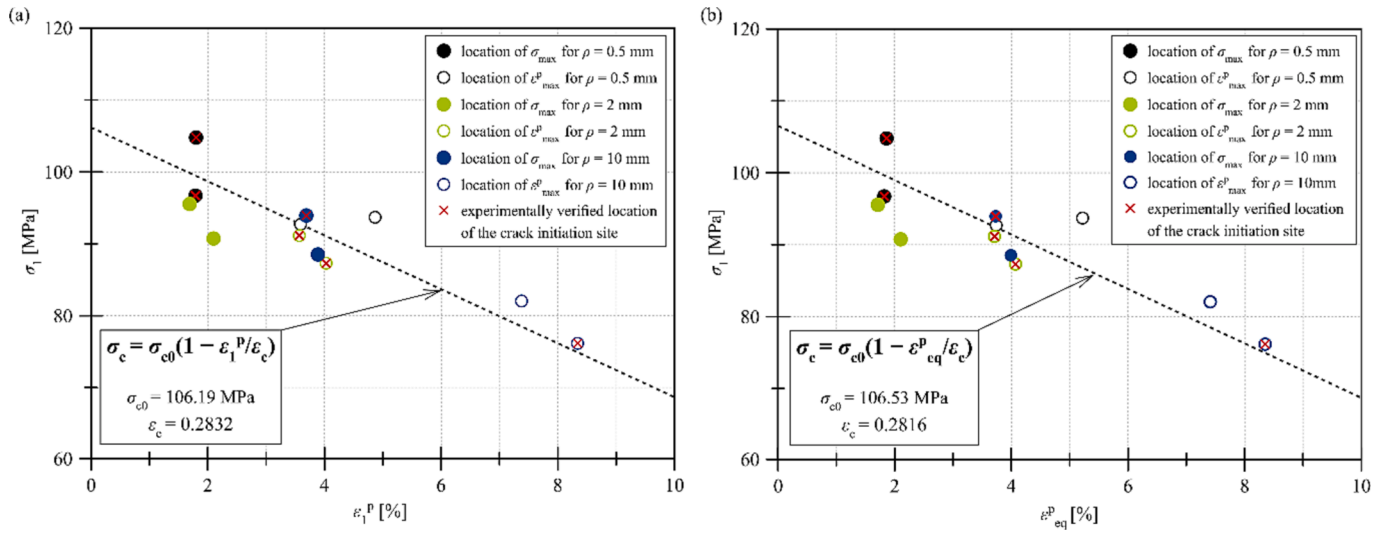

Fig. 22. The maximum principal stress σ_1 as a function of: (a) the maximum principal plastic strain ε_1^p and (b) the equivalent plastic strain ε_{eq}^p. Numerical results from the points of σ_{max} and ε_{max}^p – tension.

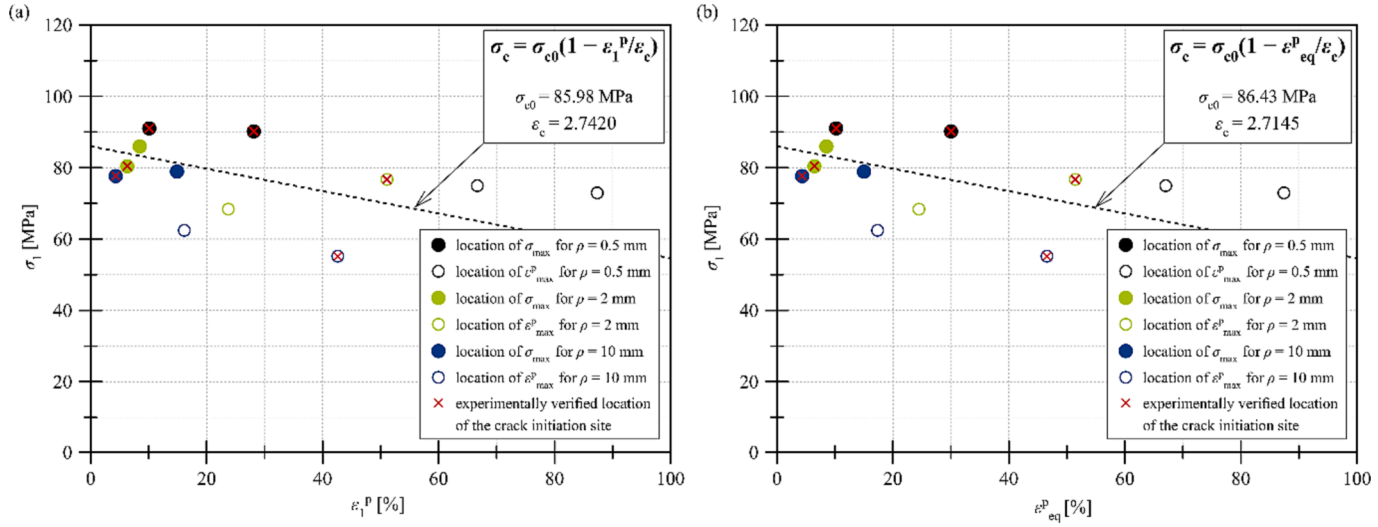

Fig. 23. The maximum principal stress σ_1 as a function of: (a) the maximum principal plastic strain ε_1^p and (b) the equivalent plastic strain ε_{eq}^p. Numerical results from the points of σ_{max} and ε_{max}^p – torsion.

state is determined at the point of occurrence of σ_{max} or ε_{max}^p. It can be concluded that the use of the above relations makes it possible to successfully predict the moment of crack initiation in flat specimens made of PMMA weakened with notches for the studied loading states. Analysing the forms of the various linear functions used to describe the relationship between the maximum principal stress and the maximum principal plastic strain (or equivalent strain), it should be noted that the relationship of these quantities for torsion specimens apparently differs from that obtained for tension elements.

6. Conclusion

The results of the studies presented in this paper, in particular the numerical modelling of the fracture of notched elements made of PMMA (based on previously conducted experimental studies) lead to a number of conclusions, which will be presented below.

1. Notched elements subjected to torsion exhibit much higher plastic deformation than for elements loaded with tensile force. The use of linear fracture mechanics calculation methods in this case can be subject to high error. Also, the failure mechanism of the specimens in the two cases is different.
2. Modelling the stress state of notched elements subjected to torsion requires the determination of a material hardening curve with a much wider range of strain than is the case in a tensile test. This relationship can be determined by a hybrid (experimental–numerical) method using the dependence of the force on the displacement of the measurement base of the notched specimen with the largest root radius.
3. Numerical modelling should also take into account small values of plastic strain (already formed above the elastic limit) and the stress redistribution caused by it, especially for notches with a small root radius subjected to tension.
4. Numerical calculations should be carried out controlling the maximum displacement (linear or angular) of the measurement base, especially in the case of torsion, for which the critical value of the torque was not always equal to the maximum value.
5. The fracture process of notched elements made of PMMA is strongly dependent on the stress state, and in particular on the maximum normal stress values. The critical value of these stress depends on the

Table 8
The stress vale σ_1, σ_{eq} and corresponding plastic strain ε_1^p measured at the point of maximum stress σ_{max} and plastic strain ε_{max}^p and the relative error for each loading condition.

ρ [mm]	g [mm]	The point of maximum stress σ_{max} value*		The point of maximum plastic strain ε_{max}^p value**		The failure stress [MPa]	The relative error [%]
		σ_{max} [MPa]	ε_1^p [%]	σ_1 [MPa]	ε_{max}^p [%]	σ_c (4)	* $\mid \sigma_{max} - \sigma_c \mid / \sigma_c$ ** $\mid \sigma_1 - \sigma_c \mid / \sigma_c$
Tension							
0.5	4.92	**96.71**	**1.79**	92.70	3.59	99.50	3*
	14.5	**104.78**	**1.80**	93.69	4.87	99.44	5*
2	4.92	90.74	2.10	**87.30**	**4.03**	91.06	4**
	14.5	95.54	1.69	**91.15**	**3.57**	92.79	2**
10	4.92	88.52	3.89	**76.16**	**8.34**	74.90	2**
	14.5	**93.95**	**3.69**	82.05	7.38	92.35	2*
Torsion							
0.5	4.92	**90.18**	**28.15**	72.93	87.37	77.15	17*
	14.5	**91.01**	**10.12**	74.95	66.69	82.80	10*
2	4.92	**80.41**	**6.32**	68.37	23.75	84.00	4*
	14.5	85.95	8.48	**76.71**	**51.11**	69.95	10**
10	4.92	**77.63**	**4.33**	62.43	16.16	84.62	8*
	14.5	78.90	14.90	**55.20**	**42.63**	71.60	24**

plastic strain. This is evident from a comparison of the critical values of normal stresses in tension and torsion. Hence, the criteria for fracture of notched elements in tension or torsion should take into account both the state of stress (in particular, the values of normal stresses) and the state of plastic deformation of the material. The relationship between the critical stress value and the value of plastic strain determined at the locations described above was described using a linear function. This enabled the formulation of a simple-to-use criterion based on the relationship between the two analysed quantities.

6. It should be noted that as a result of the nonlinear modelling of stress and strain fields using the finite element method, the maximum values of normal stresses may occur at a certain distance from the notch surface, especially in the case of tensile specimens with a larger notch root radius. Hence, fracture criteria for notched components should not be directly related to notch geometry.
7. Experimental verification showed the high effectiveness of the proposed criterion for predicting fracture in notched parts made of PMMA regardless of the specimen thickness, the notch root radius and the loading condition (tension, torsion).

Declaration of Competing Interest

The authors declare that they have no known competing financial interests or personal relationships that could have appeared to influence the work reported in this paper.

Data availability

Data will be made available on request.

Acknowledgements

This research was funded by the National Science Centre Poland based on project no 2019/33/N/ST8/02382.

References

[1] A. Seweryn, A non-local stress and strain energy release rate mixed mode fracture initiation and propagation criteria, Eng Fract Mech 59 (6) (Apr. 1998) 737–760, https://doi.org/10.1016/S0013-7944(97)00175-6.
[2] A. A. Griffith, 'VI. The phenomena of rupture and flow in solids', *Philosophical Transactions of the Royal Society of London. Series A, Containing Papers of a Mathematical or Physical Character*, vol. 221, no. 582–593, pp. 163–198, Jan. 1921, doi: 10.1098/rsta.1921.0006.
[3] A. Seweryn, A. Łukaszewicz, Verification of brittle fracture criteria for elements with V-shaped notches, Eng Fract Mech 69 (13) (Sep. 2002) 1487–1510, https://doi.org/10.1016/S0013-7944(01)00138-2.
[4] G.C. Sih, Strain-energy-density factor applied to mixed mode crack problems, Int J Fract 10 (3) (Sep. 1974) 305–321, https://doi.org/10.1007/BF00035493.
[5] G.C. Sih, B. Macdonald, Fracture mechanics applied to engineering problems-strain energy density fracture criterion, Eng Fract Mech 6 (2) (Sep. 1974) 361–386, https://doi.org/10.1016/0013-7944(74)90033-2.
[6] Z. Yosibash, A. Bussiba, I. Gilad, Failure criteria for brittle elastic materials, Int J Fract 125 (3/4) (Feb. 2004) 307–333, https://doi.org/10.1023/B:FRAC.0000022244.31825.3b.
[7] R. Lazzarin, P. Zambardi, A finite-volume-energy based approach to predict the static and fatigue behavior of components with sharp V-shaped notches, Int J Fract 112 (2001) 275–298.
[8] F. Berto, D.A. Cendon, P. Lazzarin, M. Elices, Fracture behaviour of notched round bars made of PMMA subjected to torsion at −60°C, Eng Fract Mech 102 (Apr. 2013) 271–287, https://doi.org/10.1016/j.engfracmech.2013.02.011.
[9] R.O. Ritchie, J.F. Knott, J.R. Rice, On the relationship between critical tensile stress and fracture toughness in mild steel, J Mech Phys Solids 21 (6) (Nov. 1973) 395–410, https://doi.org/10.1016/0022-5096(73)90008-2.
[10] M.R. Ayatollahi, A.R. Torabi, Brittle fracture in rounded-tip V-shaped notches, Mater Des 31 (1) (Jan. 2010) 60–67, https://doi.org/10.1016/j.matdes.2009.07.017.
[11] F.A. McClintock, Ductile fracture instability in shear, Trans. ASME, J. Appl. Mech 25 (1958) 582–588.
[12] F. Erdogan, G.C. Sih, On the Crack Extension in Plates Under Plane Loading and Transverse Shear, Journal of Basic Engineering 85 (4) (Dec. 1963) 519–525, https://doi.org/10.1115/1.3656897.
[13] F.J. Gómez, G.V. Guinea, M. Elices, Failure criteria for linear elastic materials with U-notches, Int J Fract 141 (1–2) (Sep. 2006) 99–113, https://doi.org/10.1007/s10704-006-0066-7.
[14] V.V. Novozhilov, On a necessary and sufficient criterion for brittle strength, Journal of Applied Mathematics and Mechanics 33 (2) (Jan. 1969) 201–210, https://doi.org/10.1016/0021-8928(69)90025-2.
[15] A. Seweryn, Brittle fracture criterion for structures with sharp notches, Eng Fract Mech 47 (5) (Mar. 1994) 673–681, https://doi.org/10.1016/0013-7944(94)90158-9.
[16] A. Seweryn, Z. Mróz, A non-local stress failure condition for structural elements under multiaxial loading, Eng Fract Mech 51 (6) (Aug. 1995) 955–973, https://doi.org/10.1016/0013-7944(94)00335-F.
[17] Ł. Derpeński, A. Seweryn, F. Berto, Brittle fracture of axisymmetric specimens with notches made of graphite EG0022A, Theoretical and Applied Fracture Mechanics 89 (Jun. 2017) 45–51, https://doi.org/10.1016/j.tafmec.2017.01.007.
[18] B. Saboori, A.R. Torabi, M.R. Ayatollahi, F. Berto, Experimental verification of two stress-based criteria for mixed mode I/III brittle fracture assessment of U-notched components, Eng Fract Mech 182 (Sep. 2017) 229–244, https://doi.org/10.1016/j.engfracmech.2017.06.005.
[19] B. Saboori, M.R. Ayatollahi, A.R. Torabi, F. Berto, Mixed mode I/III brittle fracture in round-tip V-notches, Theoretical and Applied Fracture Mechanics 83 (Jun. 2016) 135–151, https://doi.org/10.1016/j.tafmec.2015.12.002.
[20] M.P. Savruk, A. Kazberuk, Relationship between the stress intensity and stress concentration factors for sharp and rounded notches, Materials Science 42 (6) (Nov. 2006) 725–738, https://doi.org/10.1007/s11003-006-0140-3.
[21] M.P. Savruk, A. Kazberuk, A unified approach to problems of stress concentration near V-shaped notches with sharp and rounded tip, International Applied Mechanics 43 (2) (Feb. 2007) 182–197, https://doi.org/10.1007/s10778-007-0015-9.
[22] M.P. Savruk, A. Kazberuk, Two-dimensional fracture mechanics problems for solids with sharp and rounded V-notches, Int J Fract 161 (1) (Jan. 2010) 79–95, https://doi.org/10.1007/s10704-009-9430-8.
[23] A. Seweryn, J. Zwoliński, Solution for the stress and displacement fields in the vicinity of a V-notch of negative wedge angle in plane problems of elasticity, Eng Fract Mech 44 (2) (Jan. 1993) 275–281, https://doi.org/10.1016/0013-7944(93)90052-T.
[24] R. Bahadori, M.R. Ayatollahi, N. Razavi, F. Berto, Geometry effects on mode I brittle fracture in U-notched specimens, Fatigue Fract Eng Mater Struct 44 (4) (Apr. 2021) 901–915, https://doi.org/10.1111/ffe.13401.
[25] F. Berto, Crack initiation at V-notch tip subjected to in-plane mixed mode loading: An application of the fictitious notch rounding concept, Frattura Ed Integrità Strutturale 9 (34) (Sep. 2015), https://doi.org/10.3221/IGF-ESIS.34.18.
[26] M. Zappalorto, P. Lazzarin, F. Berto, Elastic notch stress intensity factors for sharply V-notched rounded bars under torsion, Eng Fract Mech 76 (3) (Feb. 2009) 439–453, https://doi.org/10.1016/j.engfracmech.2008.11.008.
[27] H. Talebi, M. Askari, M. Ayatollahi, S. Cicero, VO-Notches Subjected to Tension-Torsion Loading: Experimental and Theoretical Fracture Study on Polymeric Samples, Polymers (basel) 15 (11) (May 2023) 2454, https://doi.org/10.3390/polym15112454.
[28] S. Arrieta, S. Cicero, M. Sánchez, L. Castanon-Jano, Estimation of fracture loads in 3D printed PLA notched specimens using the ASED criterion, Procedia Structural Integrity 47 (2023) 13–21, https://doi.org/10.1016/j.prostr.2023.06.036.
[29] A.R. Torabi, S. Shahbaz, S. Cicero, M.R. Ayatollahi, Fracture testing and estimation of critical loads in a PMMA-based dental material with nonlinear behavior in the

presence of notches, Theoretical and Applied Fracture Mechanics 118 (Apr. 2022) 103282, https://doi.org/10.1016/j.tafmec.2022.103282.
[30] A.R. Torabi, Estimation of tensile load-bearing capacity of ductile metallic materials weakened by a V-notch: The equivalent material concept, Materials Science and Engineering: A 536 (Feb. 2012) 249–255, https://doi.org/10.1016/j.msea.2012.01.007.
[31] A.R. Torabi, M. Kamyab, The fictitious material concept, Eng Fract Mech 209 (Mar. 2019) 17–31, https://doi.org/10.1016/j.engfracmech.2019.01.022.
[32] A.R. Torabi, A.S. Rahimi, M.R. Ayatollahi, Fracture study of a ductile polymer-based nanocomposite weakened by blunt V-notches under mode I loading: Application of the Equivalent Material Concept, Theoretical and Applied Fracture Mechanics 94 (Apr. 2018) 26–33, https://doi.org/10.1016/j.tafmec.2018.01.002.
[33] B. Bahrami, M.R. Ayatollahi, A.R. Torabi, In-situ brittle fracture analysis of sharp V-notched components using digital image correlation, Theoretical and Applied Fracture Mechanics 106 (Apr. 2020) 102484, https://doi.org/10.1016/j.tafmec.2020.102484.
[34] A.R. Torabi, M. Jabbari, J. Akbardoost, Mixed mode notch fracture toughness assessment of quasi-brittle polymeric specimens at different scales, Theoretical and Applied Fracture Mechanics 109 (Oct. 2020), 102682, https://doi.org/10.1016/j.tafmec.2020.102682.
[35] A.R. Torabi, B. Saboori, S.K. Mohammadian, M.R. Ayatollahi, Brittle failure of PMMA in the presence of blunt V-notches under combined tension-tear loading: Experiments and stress-based theories, Polym Test 72 (Dec. 2018) 94–109, https://doi.org/10.1016/j.polymertesting.2018.10.002.
[36] S. Safaei, M.R. Ayatollahi, B. Saboori, Fracture behavior of GPPS brittle polymer under mixed mode I/III loading, Theoretical and Applied Fracture Mechanics 91 (Oct. 2017) 103–115, https://doi.org/10.1016/j.tafmec.2017.04.017.
[37] B. Saboori, A. R. Torabi, and S. Keshavarz Mohammadian, 'Experimental and stress-based theoretical studies on mixed mode I/III fracture of round-tip V-notched Polystyrene specimens', *Theoretical and Applied Fracture Mechanics*, vol. 95, pp. 283–305, Jun. 2018, doi: 10.1016/j.tafmec.2018.03.008.
[38] M.R. Ayatollahi, B. Saboori, A new fixture for fracture tests under mixed mode I/III loading, European Journal of Mechanics - A/solids 51 (May 2015) 67–76, https://doi.org/10.1016/j.euromechsol.2014.09.012.
[39] E. Bura, A. Seweryn, Mode I fracture in PMMA specimens with notches – Experimental and numerical studies, Theoretical and Applied Fracture Mechanics 97 (Oct. 2018) 140–155, https://doi.org/10.1063/1.4992645.
[40] X. Chen, A. Doitrand, N. Godin, C. Fusco, Crack initiation in PMMA plates with circular holes considering kinetic energy and nonlinear elastic material behavior, Theoretical and Applied Fracture Mechanics 124 (Apr. 2023), 103783, https://doi.org/10.1016/j.tafmec.2023.103783.
[41] A. Doitrand, G. Molnár, D. Leguillon, E. Martin, N. Carrère, Dynamic crack initiation assessment with the coupled criterion, European Journal of Mechanics - A/solids 93 (May 2022) 104483, https://doi.org/10.1016/j.euromechsol.2021.104483.
[42] E. Bura, Ł. Derpeński, A. Seweryn, Fracture in PMMA notched specimens under compression – Experimental study, Polym Test 77 (Aug. 2019) 105923, https://doi.org/10.1016/j.polymertesting.2019.105923.
[43] E. Bura, A. Seweryn, Fracture Initiation in Notched Specimens Subjected to Compression: Strain Rate Effect, Materials 13 (11) (Jun. 2020) 2613, https://doi.org/10.3390/ma13112613.
[44] A. Leite, V. Mantič, F. París, Crack onset in stretched open hole PMMA plates considering linear and non-linear elastic behaviours, Theoretical and Applied Fracture Mechanics 114 (Aug. 2021) 102931, https://doi.org/10.1016/j.tafmec.2021.102931.
[45] E. Bura, A. Seweryn, The fracture behaviour of notched PMMA specimens under simple loading conditions – Tension and torsion experimental tests, Eng Fail Anal 148 (Jun. 2023) 107199, https://doi.org/10.1016/j.engfailanal.2023.107199.
[46] A. Seweryn, Z. Mróz, On the criterion of damage evolution for variable multiaxial stress states, Int J Solids Struct 35 (14) (May 1998) 1589–1616, https://doi.org/10.1016/S0020-7683(97)00121-2.
[47] L. Derpenski, A. Seweryn, Ductile fracture of EN-AW 2024 aluminum alloy specimens with notches under biaxial loading. Part 2 – Numerical research and ductile fracture criterion, Theoretical and Applied Fracture Mechanics 84 (Aug. 2016) 203–214, https://doi.org/10.1016/j.tafmec.2016.06.008.
[48] L. Derpenski, A. Seweryn, Ductile fracture of EN-AW 2024 aluminum alloy specimens with notches under biaxial loading. Part 1 – Experimental research, Theoretical and Applied Fracture Mechanics 84 (Aug. 2016) 192–202, https://doi.org/10.1016/j.tafmec.2016.06.007.
[49] Ł. Derpeński and A. Seweryn, 'Ductile fracture criterion for specimens with notches made of aluminium alloy EN-AW 2024', *Journal of Theoretical and Applied Mechanics*, p. 1079, Dec. 2016, doi: 10.15632/jtam-pl.54.4.1079.
[50] Ł. Derpeński, A. Seweryn, J. Bartoszewicz, Ductile fracture of notched aluminum alloy specimens under elevated temperature part 1 – Experimental research, Theoretical and Applied Fracture Mechanics 102 (Aug. 2019) 70–82, https://doi.org/10.1016/j.tafmec.2019.04.001.
[51] Ł. Derpeński, A. Seweryn, Ductile fracture of notched aluminum alloy specimens under elevated temperature part 2 – Numerical modelling and fracture criterion, Theoretical and Applied Fracture Mechanics 102 (Aug. 2019) 83–97, https://doi.org/10.1016/j.tafmec.2019.01.023.
[52] M. A. Azizi, M. F. M. Ridhuan, M. Z. M. Zahari, S. A. Rahim, and M. A. Azman, 'Peridynamic Model for Tensile Elongation and Fracture Simulations of Polymethyl Methacrylate Notched Specimens', *Applied Mechanics and Materials*, vol. 909, pp. 11–28, Sep. 2022, doi: 10.4028/p-2z0841.